CHALMERS

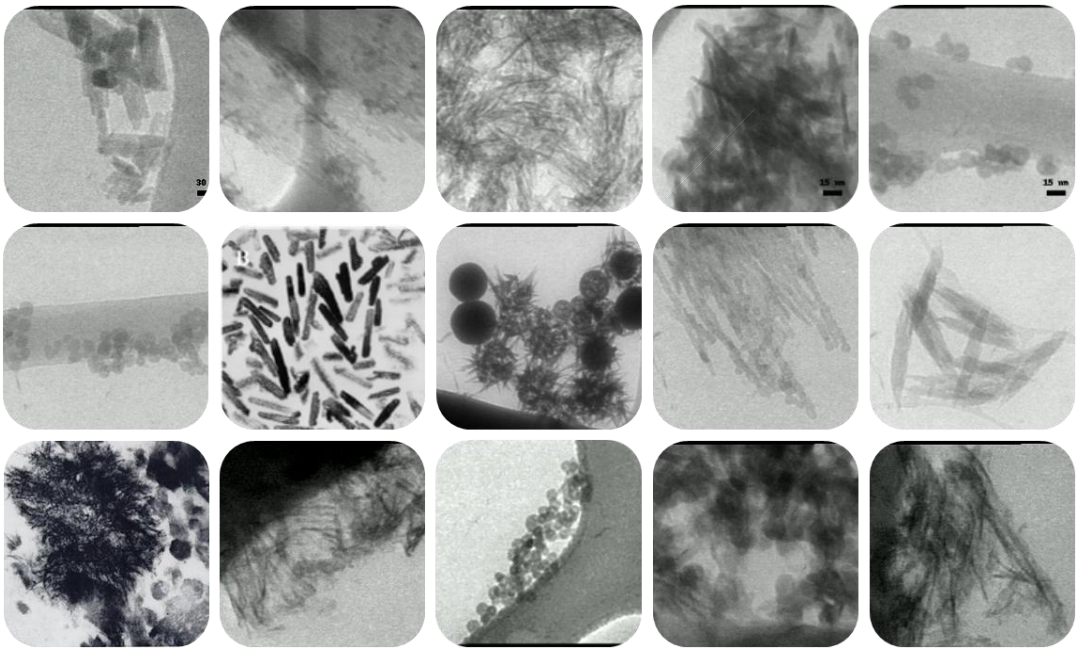

Synthesis of Bone-like Apatite
Using Liquid Crystalline Phases as Templates

Master of Science Thesis [The Materials and Nanotechnology Program]

WENXIAO HE

Department of Chemical and Biological Engineering
Division of Applied Surface Chemistry
CHALMERS UNIVERSITY OF TECHNOLOGY
Göteborg, Sweden, 2010

THESIS FOR THE DEGREE OF MASTER OF SCIENCE

Synthesis of Bone-like Apatite
Using Liquid Crystalline Phases as Templates

Wenxiao He

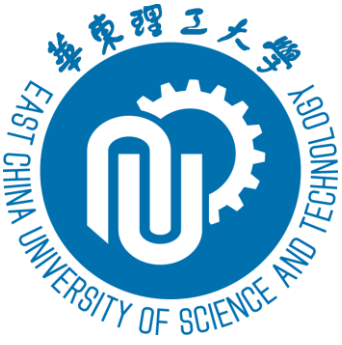

Supervised by Martin Andersson

Department of Chemical and Biological Engineering
CHALMERS UNIVERSITY OF TECHNOLOGY

Göteborg, Sweden 2010

Synthesis of Bone-like Apatite Using Liquid Crystalline Phases as Templates

Department of Chemical and Biological Engineering
Chalmers University of Technology
SE-412 96 Göteborg
Sweden
Telephone + 46 (0)31-772 1000

Cover: TEM micrographs of various nanocrystalline apatites and amorphous calcium phosphate templated by liquid crystalline phases or found in calcified tissues. By manipulating the condition of synthesis and subsequent maturation, calcium phosphate with distinct morphology and crystallinity can be prepared.

Göteborg, Sweden 2010

Synthesis of Bone-like Apatite Using Liquid Crystalline Phases as Templates

Wenxiao He

Applied Surface Chemistry
Department of Chemical and Biological Engineering
CHALMERS UNIVERSITY OF TECHNOLOGY

Abstract

The mineral phase in bone is nanocrystalline apatite, which is –OH deficient, CO_3– substituted and poorly crystalline. Recent efforts have been devoted to form such particles synthetically for hard tissue engineering applications. Liquid crystalline phases (LCP) having water domains in the size range 5–10 nm can be used as templates for the synthetic preparation of nano-sized apatite.

In this project, LCPs together with Glycosaminoglycans (GAGs) have been utilized for the synthesis of nano-sized apatite. The mineral was formed using a LCP having a reverse hexagonal structure. Without any post procedures, the formed material was amorphous calcium phosphate (ACP) spheres with a diameter of 8 – 12 nm. With a controlled post process, the ACPs gradually dissolved and crystallized to form nano-sized hydroxyapatite (HA). This ACP to HA conversion was H_2O mediated and temperature dependent. The addition of GAGs was also explored during aging. GAG's were used since the carboxyl and sulphate groups on GAGs are known to interact electrostatically with the calcium sites on HA. GAGs were shown to have a hindering effect on the ACPs' crystallization.

The HA formed using LCPs were compared to HA formed using simple water based precipitation (WBP). With the regulation of the LCP, proper aging process and the modulation of GAGs, needle-like apatites having bone resembling features, such as Ca and OH– deficiencies, CO_3^{2-} substitution, poor crystallinity and with a very high specific surface area were formed.

The formed LCP structures were examined by Polarized Light Microscopy (PLM) and Small Angle X-ray Scattering (SAXS). Transmission Electron Microscopy (TEM) was used to follow the particle formation inside LCP and the aging process in H_2O media. Obtained particles were characterized by Nitrogen Adsorption, Powder X-ray Diffraction (XRD) and TEM, for their specific surface area, crystal structure and morphology. The GAGs – HA interaction was examined using Quartz Crystal Microbalance with Dissipation Monitoring (QCM-D). Complementary techniques such as Thermal Gravimetric Analysis (TGA) and Raman Spectroscopy, etc. were also used for the comparison between the prepared LCP and WBP samples.

Keywords Nanocrystalline apatite, Liquid crystalline phase, Glycosaminoglycans (GAGs), Pluronic L64, ACP – HA conversion

List of Abbreviations

ACP	Amorphous Calcium Phosphate
BET	Brunauer-Emmett-Teller (Specific Surface Area Analysis)
C4S	Chondroitin-4-Sulfate
EDS	Energy Dispersive Spectroscopy
GAGs	Glycosaminoglycans
H_1	Normal Hexagonal Phase
H_2	Reverse Hexagonal Phase
HA	Hydroxyapatite
L_a	Lamellar Phase
LCP	Liquid Crystalline Phase
NCP	Non-collagenous Protein
PCA	Poorly Crystallized Apatite
PG	Proteoglycan
PLM	Polarized Light Microscopy
QCM-D	Quartz Crystal Microbalance with Dissipation Monitoring
SAXS	Small Angle X-ray Scattering
SEM	Scanning Electron Microscopy
TEM	Transmission Electron Microscopy
TCP	Tricalcium Phosphate
TGA	Thermal Gravimetric Analysis
TGA-IR	Thermogravimetry with Infrared-Coupling
WBP	Water Based Precipitation
XRD	X-ray Diffraction

Contents

1 Introduction

Bone is a ubiquitous composite material with an ingenious hierarchical structure [1], which results in its sublime mechanical, biochemical and metabolic properties. The bone matrix is an interpenetrating network composed of organic and inorganic constituents. The organic part formed by type I collagen, small quantities of noncollagenous proteins (NCPs, such as osteocalcin, osteonectin, proteoglycans, etc. [2]) and glycosaminoglycans (GAGs), offers elasticity to the bone as well as compressive, tensile and fractural resistance. While the inorganic part, which is made of bone mineral (up to 60 wt%) and water, provides the toughness and pressure bearing capacity.[3]

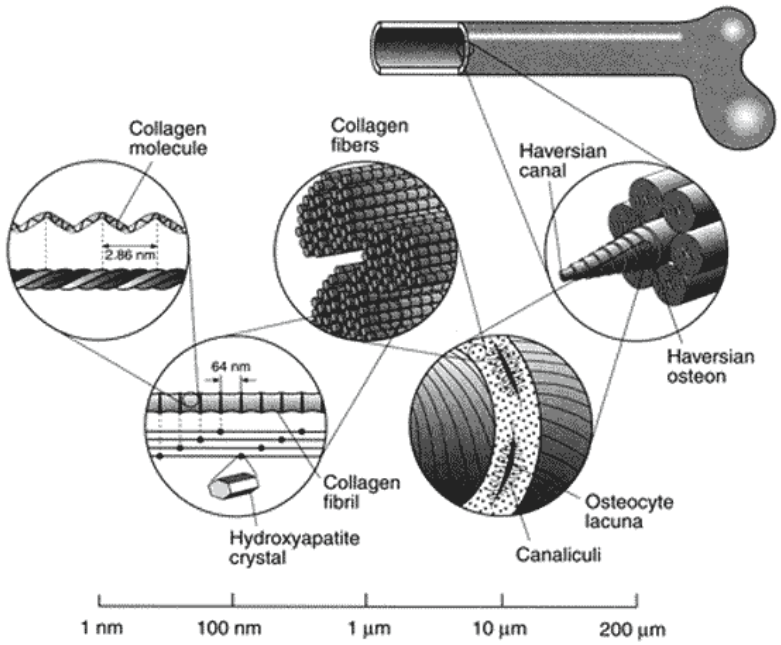

Figure 1: Hierarchy of the bone structure.[4]

Fig.1 shows the different levels of the bone structure. At the molecular level, a triple-helix collagen molecule is self-assembled from three coiled polypeptide chains. These collagen molecules aggregate into fibrils in a staggered manner. Within the fibrillar framework, bone mineral is deposited. At the micro-scale, these mineralized fibrils conglomerate into collagen fibers, which are further lined in arrays and forming woven or lamellar bone. The type of bone depends on the alignment of collagen.[5]

1.1 Bone Apatite

Due to chemical and crystallographic resemblance, bone mineral is normally referred to as hydroxyapatite (HA). However, comparing bone mineral to geological and synthetic HA, bone apatite has unique features, such as calcium and hydroxyl group deficiencies, carbonate substitution (4 – 8 wt%), nanometric dimension as well as poor crystallinity. These features of bone apatite together with the elaborate composite structure (i.e. the distributed mineralization within the collagen matrix) not only make bone a splendid structural material, but also confer bone resorbability and

regenerability.[3, 6]

The formation of bone apatite is a highly controlled and modulated process.[7] Rod-like collagen molecules align themselves in a quarter-staggered manner, which causes periodic gaps and overlap zones. These are the exact locations where mineralization occurs. Bone apatite either forms in the gap zone (28 wt%) or epitaxially grows in/on the fibrils (58 wt% for radially intrafibrillar growth while 14 wt% for interfibrillar growth, see Fig.2).[8] During this process, the minor components namely NCPs and GAGs play significant roles in specifically locating/providing nucleation sites on collagen fibrils and subsequently regulating crystal growth rate and size.

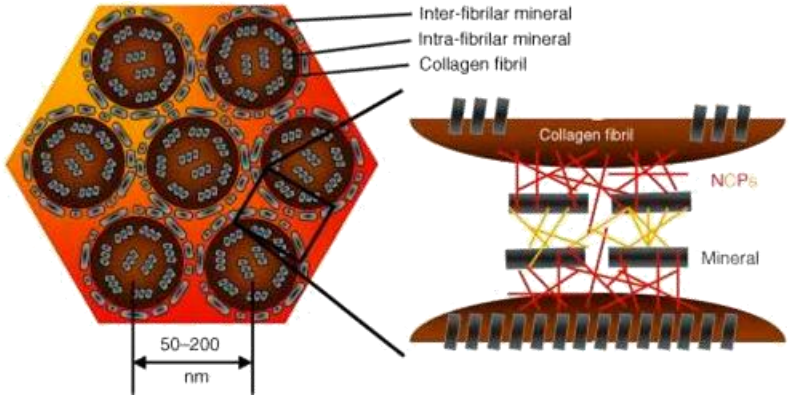

Figure 2: Schematic model of bone mineral positions.[9]

1.2 Synthetic Attempts Toward Forming Bone-like Apatite

Recent efforts have been devoted to form bone-like apatite synthetically for hard tissue engineering applications. The main criteria for bone-like apatites are the small crystal size, calcium deficiency and carbonate substitution. There are two main tactics for their formation that can be utilized.[3] One is to use wet chemical methods to synthetically prepare HA particles with small crystal size, while the other involves the utilization of physiological body fluids or collagen substrates [10]. This latter method is often referred to as a biomimetic formation procedure.

Various routes had been employed to obtain HA nano-particles, including water based precipitation (WBP), precipitation using emulsions, micro-wave synthesis, aerosol synthesis, mechano-chemical process, templates and sol-gel techniques, etc.[11-15]

1.3 Project Work

The purpose of this project was to prepare nanometric apatite morphologically and compositionally similar to bone apatite for an improved performance in biomedical applications.

By studying the process of bone mineralization, two key factors in bone apatite formation have to be considered. Specifically, the confined space afforded by the collagen matrix, and the modulation of biomacromolecules like NCPs and GAGs. Therefore, in the present study two elements were adopted to mimic this natural

formation procedure; the liquid crystalline phase (LCP) as template for size confinement and the addition of GAGs for structural regulation. The experimental part that was implemented followed three stages:

i. Investigation of the formation of nanocrystalline apatites using LCP templating systems, especially the reverse hexagonal phase.

ii. The examination of GAGs effect during the formation of nanocrystalline apatite.

iii. The comparison between apatites formed by the LCP route and conventional water based precipitation.

2 Theory

2.1 Hydroxyapatite

Hydroxyapatite has the chemical formula $Ca_5(PO_4)_3OH$ (can also be written as $Ca_{10}(PO_4)_6(OH)_2$), which gives a theoretical Ca/P ratio of 1.67. HA is one of the most common and most stable forms of calcium phosphate. The crystal system of HA is hexagonal-dipyramidal (space group $P6_3/m$) with crystallographic parameters, a = 9.418 Å, c = 6.881 Å, β = 120 °.[16]

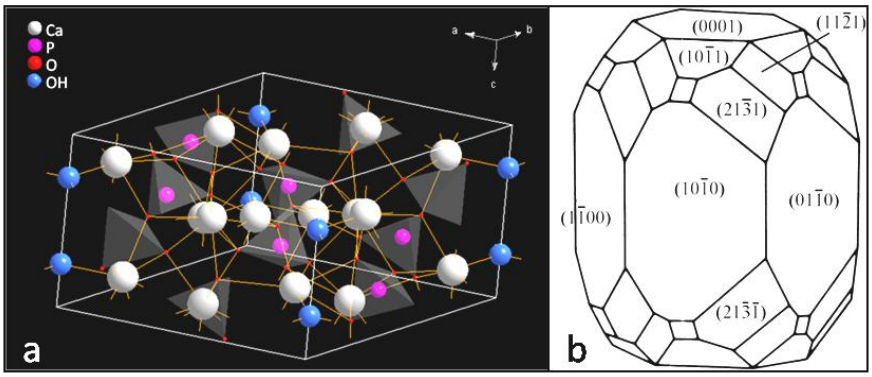

Figure 3: Crystal structure (a) and morphology (b) of hydroxyapatite [17].

The crystal structure of HA (Fig.3) is composed of ordered stacks of phosphate groups, which are forming two sorts of locations for Ca^{2+} ions within two different channels parallel to the c axis. The size of these channels are 3 Å and the structure confers ion exchange properties upon HA, which makes it quite substitution-tolerant while retaining the crystal structure.[18] As a consequence of this substitution, the possible vacancies in the HA structure produces non-stoichiometry, which results in a OH-deficiency, low crystallinity and relatively high solubility. The maturation of HA in an aqueous solution will decrease its non-stoichiometry.

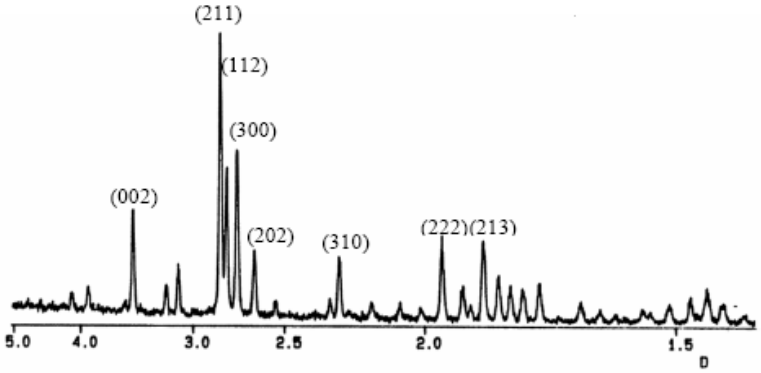

Figure 4: X-ray diffraction diagram of hydroxyapatite [JCPDS No. 9-432].[19]

Well-crystallized HA (XRD pattern is seen in Fig.4) has a relatively high thermostability. The dehydroxylation of HA starts at high temperatures (over 1000 ℃) and result in oxyhydroxyapatite (OHA) [20]:

$$Ca_{10}(PO_4)_6(OH)_2 \underset{900\,℃}{\overset{1000\text{-}1360\,℃}{\rightleftharpoons}} Ca_{10}(PO_4)_6(OH)_{2-2x}O_x + xH_2O$$

Further heating causes the decomposition of HA, whereby it transforms to tetracalcium phosphate (TTCP) and α-tricalcium phosphate (α-TCP):

$$Ca_{10}(PO_4)_6(OH)_{2-2x}O_x \underset{\sim 1360\,℃}{\overset{>1360\,℃}{\rightleftharpoons}} Ca_4(PO_4)_2O + 2\alpha\text{-}Ca_3(PO_4)_2 + (1\text{-}x)H_2O$$

Various approaches can be used for the preparation of HA, among which water-based co-precipitation is the most commonly used. It includes the double decomposition of calcium and phosphorous salts and a neutralization reaction.[19, 21] Methods such as solid phase reactions, sol-gel processes, hydrothermal reactions and so on can also be used.[11, 15, 58]

As an analogue to bone apatite, HA particles have been widely used in the biomedical fields as drug carriers for controlled release, implant coatings and as fillers for bone substitutes. The usage is driven by the materials high biocompatibility and bioactivity. Additionally, the biological efficacy is closely related to the HA particle size. Nano-sized apatite particles often perform better due to their high specific surface area and to their similarity to bone apatite, both in terms of morphology and composition. Studies has shown that bone forming cells exhibit excellent attachment and proliferation on nanosized apatite surfaces and that they are triggered to form new bone.[12]

2.2 ACP – HA Conversion

In the early stage of bone and teeth mineralization, an amorphous phase has been observed instead of crystallized apatite.[22, 23] It can be seen as electron-dense spherical regions in TEM micrographs [24] (dashed circles in Fig.5) and presents a broad halo centered at $2\theta = 36.5$ in XRD patterns (see Fig.6). This transient precursor of amorphous calcium phosphate (ACP), with relatively low Ca/P ratio and high HPO_4^{2-} content,[25] will undergo an autocatalytic phase transformation [26] to form poorly crystallized apatite (needle-like particles, indicated by arrows in Fig.5) when present in aqueous medium.[27]

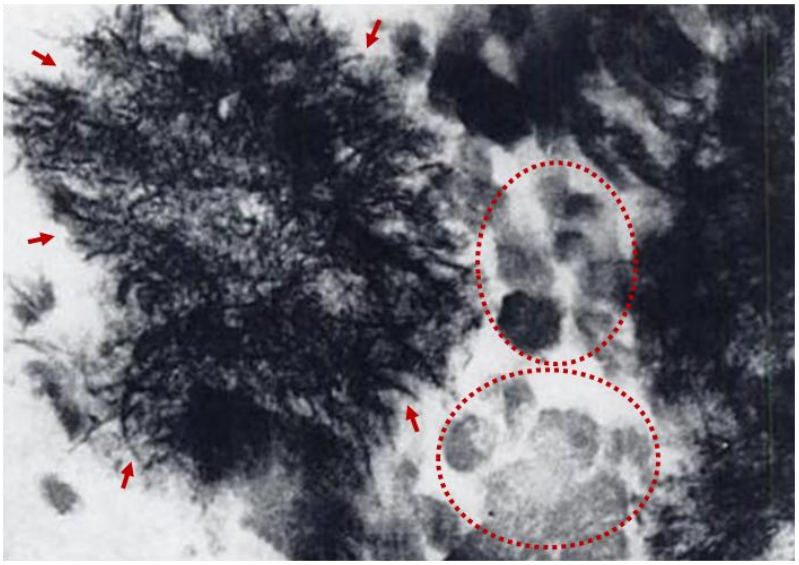

Figure 5: Calcification nodule in a bone section, original magnification×125,000.[28]

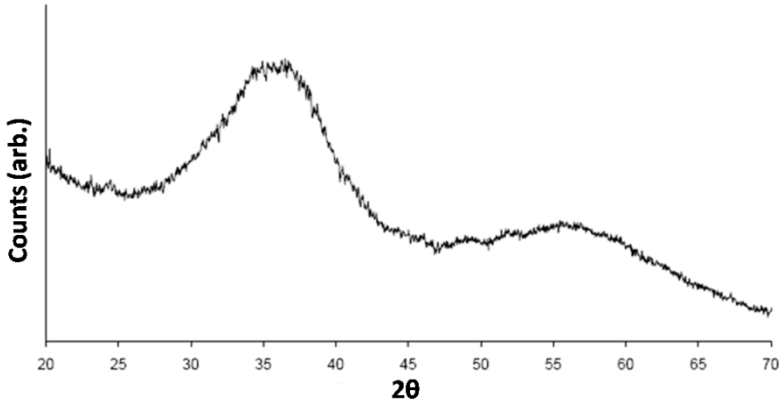

Figure 6: XRD pattern of ACP.[19]

The underlying mechanism of ACP – HA conversion is suggested as a dissolution/re-precipitation phenomenon [29, 30] or as a rearrangement of the Posner's clusters $Ca_9(PO_4)_6$ (diameter 9.5Å) [31, 32] accompanying by the hydrolysis of internal phosphate ions.

$$PO_4^{3-} + H_2O \longrightarrow HPO_4^{2-} + OH^-$$

The ACP – HA conversion rate can be influenced by several factors, such as temperature, pH, existence of impurity ions or biomacromolecules, organic co-solvents and the concentration of mother solution. For instance, high temperature, acidic/neutral environment and high concentration of slurry benefit the conversion to different extent.[30, 33, 34] Besides, under low pH, other transient phases such as octacalcium phosphate or brushite might occur before HA is formed. ACPs are fairly stable at a cool, basic medium. The presence of ions such as Mg^{2+}, Al^{3+}, CO_3^{2-}, $P_2O_7^{4-}$ and so on may also hinder the conversion.

2.3 Liquid Crystalline Phases

Liquid crystalline phases (LCP) are intermediate structures (meso-phases) between liquids and periodic crystals.[35] Liquid crystals have a certain degree of fluidity, while at the same time having a short-range order. They exist extensively in nature, for instance, biopolymers (e.g. DNA molecules, peptides, glycopolymers etc. [36]) tend to aggregate and form fibrillar structures, which can further orient and pack into LCPs in aqueous media when certain concentrations have been reached (see Fig.7).

Surfactants have the ability to form complex LCPs in aqueous solution (lyotropic LCP). The underlying mechanism for this self-assembly process is the competition between the hydrophilic and hydrophobic portions within the surfactant molecule (amphiphilic organic molecule). The critical packing parameter (CPP), which is the ratio of effective volume *v*, hydrophilic head area *a* and chain length *l* of a surfactant is quite crucial in the types of LCPs that they might form (see Fig.8).

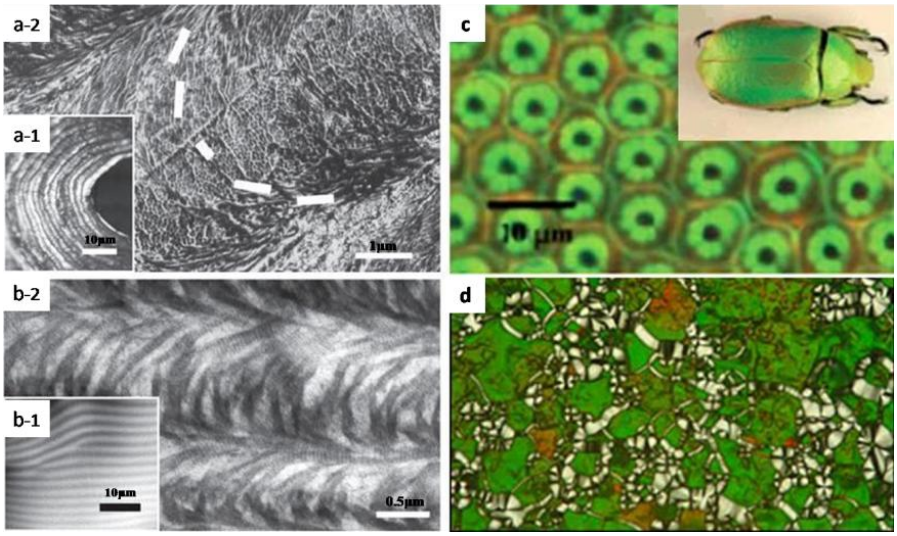

Figure 7: Collagen super-molecular structure (human compact bone osteon, a-1, a-2: TEM), liquid crystalline collagen assemblies (b-1: PLM, b-2: TEM), iridescent forewings of Plusiotis boucardi beetle (helicoidal stacking of fibrous chitin layers vaused coloring, c) and LCP formed by DNA molecules in solution (d: PLM).[37-39]

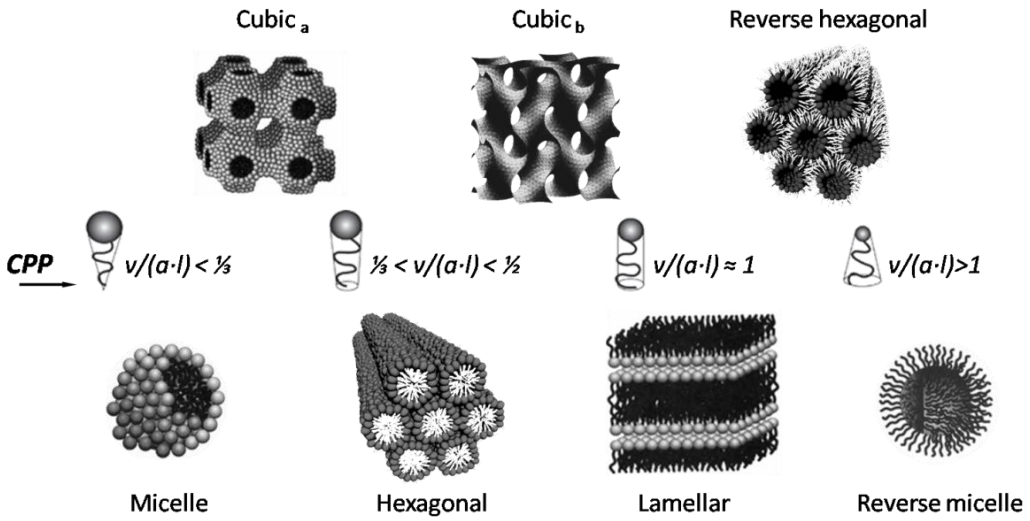

Figure 8: Various LCPs formed by surfactants with different CPPs.

LCPs have aroused appreciable interests in fabricating materials with sophisticated architectural features at the nanoscale. The confined meso-structures of lamellar, cubic and hexagonal phases have been widely utilized as templates for the synthesis of mesoporous materials. The general approach is to form LCPs with the help of surfactants, followed by the reaction of soluble precursors contained in the restricted water domains, yielding the wanted inorganic material. The adoption of block copolymers as templating agents in this strategy has greatly diversified the attained structure and the range of inorganic materials. The EO–PO triblock copolymers (trade name: Pluronic®), in particular, are commonly used. Pluronics are nonionic, which results in phases that are less sensitive to salt additions and temperature changes. An example of a Pluronic phase diagram is presented in Fig.9.

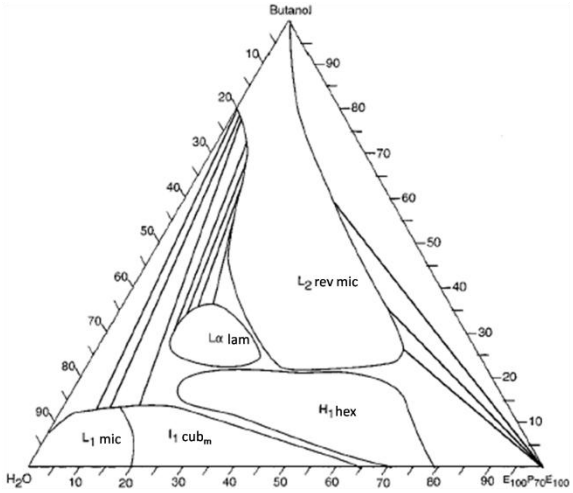

Figure 9: Ternary phase diagram of the $EO_{100}PO_{70}EO_{100}$-butanol-water system.[59]

2.4 Glycosaminoglycans

Glycosaminoglycans (GAGs) are a family of sulphated (except hyaluronan) linear polymers with repeating disaccharide building blocks. The variable backbones, sulphation sites and spatial arrangements on the sugar chain confer GAGs structural diversification,[40] thus render GAGs the ability to covalently bind to different proteins to form proteoglycans (PGs).

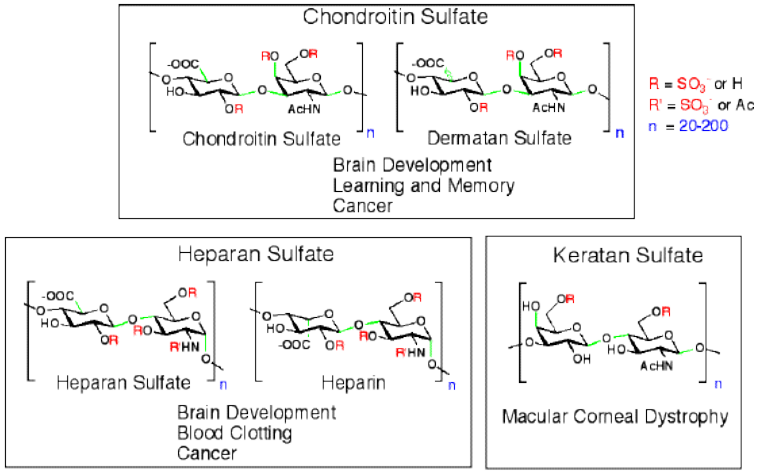

Figure 10: Examples of GAG families.[41]

GAGs abundantly exist in the body. Chondroitins as the most prevalent GAG can be found in cartilage. Heparin, the anticoagulant is located in the blood vessels of organs like lungs and liver. Hyaluronan functions as lubricant in the extracellular matrix of connective tissue.[41]

The GAGs, chondroitin, keratan and dermatan sulfate also exist in the bone matrix. PGs with different GAG chains play significant roles in regulating bone mineralization in terms of nucleation location, crystal growth, composition, morphology and orientation.[42, 43] There are electrostatic interactions between the anionic sites (carboxyl or sulphate groups) on GAGs and the cationic sites (calcium) on HA,[44] which facilitate the multi-point binding of GAGs/PGs onto HA. The

nucleation of HA takes place in either matrix vesicles or collagen fibrils. In the latter case, PGs interact with collagen fibrils providing specific locations to attract Ca^{2+} and PO_4^{3-} ions, initiating the mineralization.[45] While the inhibitory and modulating mechanism of HA crystal growth and spatial delineation is a combination of steric hindrance caused by accumulated PGs and the calcium chelation as a result of the affinity between GAGs and HA.[42] Thus, bone apatites with extremely small crystal size at specific locations are formed.

2.5 Characterization

2.5.1 Polarized Light Microscopy

Polarized light microscopy (PLM) is a technique where a transmission optical microscope equipped with two polaroid filters that are aligned perpendicular to each other is used. If there is an isotropic and transparent sample placed between the two filters, no image can be seen in the ocular, since the two polarizers will block the light. Whereas if the sample is anisotropic, which means it can change the direction of polarized light that passes through, specific patterns with respect to structure induced birefringence of the sample can be observed. Therefore, PLM is an effective way for identifying LCPs (see Fig.11).

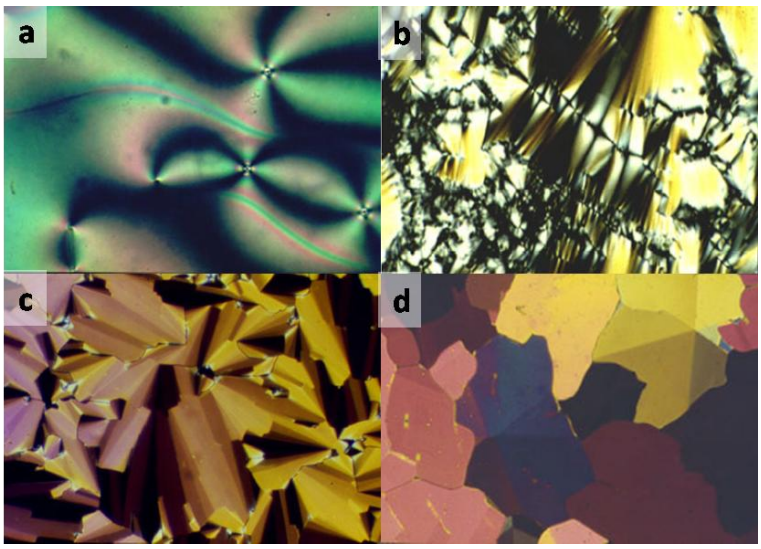

Figure 11: PLM images for different LCPs: a-nematic, b-lamellar, c-hexagonal and d-mosaic textures of soft LCPs.[46]

2.5.2 Small-angle X-ray Scattering

Small-angle X-ray scattering (SAXS) is an accurate technique used for detecting structural features at the mesoscale (1nm up to 50nm). The principle is to beam X-rays (with wavelength 1~2Å) towards materials at low angles (<10 °), followed by evaluating the out-coming scattering patterns to obtain morphological information such as particle size, pore distribution and other parameters.

SAXS can also be used to determine the structure of systems having long-range order, like LCPs. Fig.12 shows three SAXS profiles related to different LCPs. By calculating

the ratio of distance between different peaks, one can easily tell the phase structure of the system. The lamellar phase, noted L_α, has the same distance between adjacent peaks (Fig. 12A). Hexagonal phases (H_1/H_2 represents normal/reverse hexagonal phase respectively) is characterized by peak position ratio of 1, $\sqrt{3}$, 2, $\sqrt{7}$…(Fig.12, B). More details are shown in table 1.

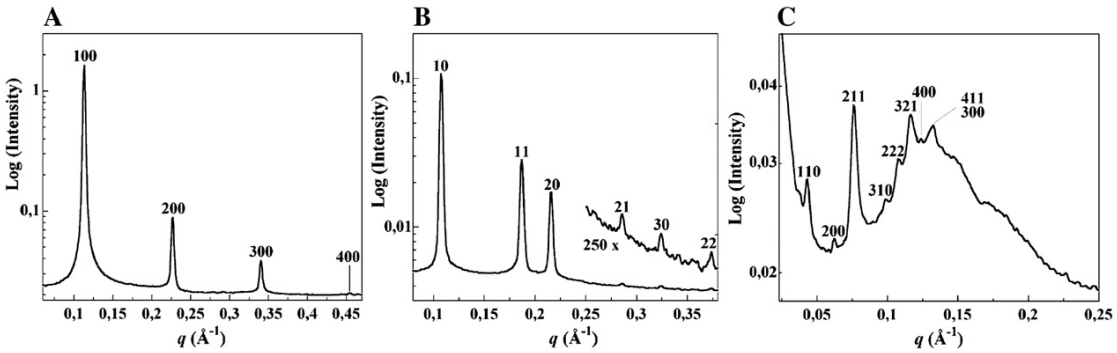

Figure 12: SAXS patterns of the galactolipid/water systems with different LCP structure: A-lamellar, B-hexagonal and C-cubic phase.[47]

Table 1: SAXS calculation of LCPs.[47]

Lamellar Phase				Hexagonal Phase				Cubic Phase			
h	*k*	*l*	*n*	*h*	*k*	*l*	*n*	*h*	*k*	*l*	*n*
1	0	0	1	1	0	0	1	1	1	0	2
2	0	0	2	1	1	0	3	1	1	1	3
3	0	0	3	2	0	0	4	2	0	0	4
4	0	0	4	2	1	0	7	2	1	1	6
$q_n=2\pi n/d_{lam}$				$n=h^2+hk+k^2$ $q_n=4\pi\sqrt{n}/\sqrt{3}d_{hex}$				$n=h^2+k^2+l^2$ $q_n=2\pi\sqrt{n}/d_{cub}$			

n: Bragg reflection order
d: lattice parameter (nearest-neighbor distance)
q_n: Theoretical peak position of small angle reflections

For hexagonal phase, the cross section radius R_{cyl} of cylindrical domains can be further calculated by the following equation (Φ_{cyl}: volume fraction) [48],

$R_{cyl} = d_{hex}((\sqrt{3}/2\pi)\,\Phi_{cyl})^{1/2}$.

2.5.3 X-ray Diffraction

X-ray Diffraction (XRD) is a method for acquiring the atomic placement and crystallographic information of crystalline materials. The basic principle is to use a gradually rotated beam of X-rays to continually bombard a crystal to produce a diffraction pattern with contrastable intensities. At certain incident angles, the ordered array of waves reflected by the atomic plane in a crystallite will achieve constructive interference and leave an intensity peak on the XRD curve. Bragg's law is used to describe this condition, by which the *d*-spacing between atomic planes can be calculated,

$2d\sin\theta = n\lambda$, where *n* is any integer, θ *and* λ is the angle and wavelength of the incident beam.

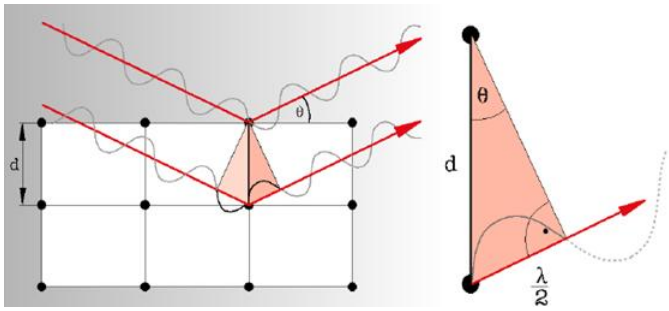

Figure 13: Schematic illustration for diffraction of X-rays.[49]

One of the most important applications of XRD is to compare obtained data with the JCPDS (Joint Committee on Powder Diffraction Standards) cards to find the crystal structure of the investigated material. Peak information like Full Width at Half Maximum (FWHM) can be used as compliment way to get particle/grain size using the Scherrer equation,

$\tau = K\lambda / (\beta \cos\theta)$,

where K is the shape factor (typical around 0.9), λ and θ is the wavelength and angle of incident beam, β is FWHM in radians.

2.5.4 Transmission Electron Microscopy

Electron microscopy shares basic principles with optical microscopy, but uses electrons as source instead of photons. The reason for this is that the extremely small wavelength of electrons (0.004 nm for a 100 KeV electron) compared to visible light (400 – 700 nm), which can provide a much superior resolution (~ 0.1 nm for TEM). TEM is a convenient yet comprehensive technique for detecting morphological, crystallographic and compositional information of materials. The principle is to let a focused beam of electrons pass through (also interact with) the specimen resulting in a two dimensional magnified projection onto a fluorescent screen. Thus the sample needs to be very thin (~ 100 nm) and the TEM columns should be under high vacuum to prevent the disturbance and hindrance of the electron beams.

There are several kinds of interactions of electrons with the specimen. Among which, the elastically scattered and diffracted electrons are respectively responsible for bright field and dark field image formation. TEM can also be combined with spectroscopy, such as EDS (Energy Dispersive X-Ray Spectroscopy) and EELS (Electron Energy Loss Spectroscopy), to provide chemical or atomic compositional information and so on.

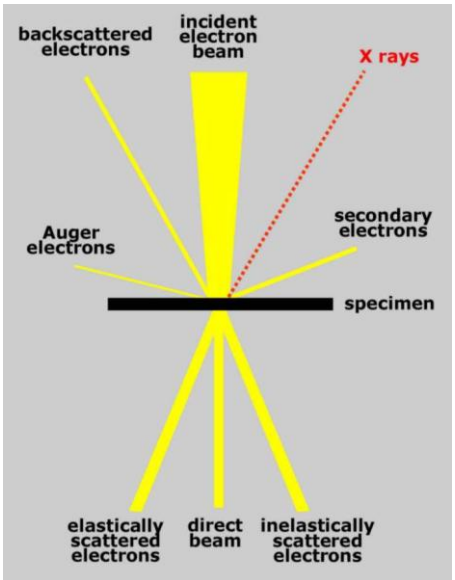

Figure 14: Electron interactions in TEM.[50]

2.5.5 Nitrogen Adsorption

Nitrogen adsorption is a favourable method for acquiring the specific surface area and porosity characteristics of solid materials. The theory applied for the correlation between the amount of adsorbed gas molecules and specific surface area is the BET method proposed by Brunauer, Emmett, and Teller in 1938.[51] As an extension of the Langmuir isotherm (monolayer adsorption of molecules, suits for chemisorption), BET theory set a model for multilayer adsorption (physisorption) by assuming "no interaction between each adsorption layer and that the Langmuir theory can be applied to each layer". The resulting equation is,

$$\frac{1}{v[(P_0/P)-1]} = \frac{c-1}{v_m c}\left(\frac{P}{P_0}\right) + \frac{1}{v_m c} \ ,$$

where P and P_0 is the pressure of N_2 when equilibrium and saturation is reached, respectively. v is the volume adsorbed (subscript m means monolayer) and c is the BET constant related to the adsorption enthalpy.

The specific surface area, S, can be calculated by,

$$S_{BET} = \frac{v_m N_A a_m}{m v_l} \ ,$$

where N_A is Avogadro number, a_m is the adsorption cross section by each N_2 molecule (16.2 $Å^2$ for N_2), v_l the molar volume of N_2 and m is the sample weight.

2.5.6 Quartz Crystal Microbalance with Dissipation Monitoring

Quartz Crystal Microbalance with Dissipation Monitoring (QCM-D) is a real time surface sensitive technique employed for studying adsorption/desorption behaviors as well as surface reactions on a thin film in liquid or air. The core of this technique is the piezoelectricity of a quartz crystal, which enables the shear-mode oscillation of a QCM-D disc under applied voltage.

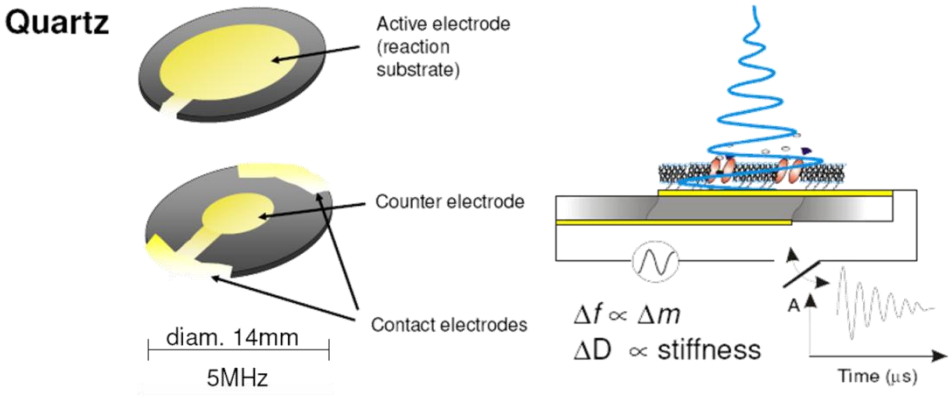

Figure 15: QCM-D disc and working principle.[52]

Fig. 15 illustrates the basic principle of this weighing balance. Two parameters are monitored during the resonation of the disc, namely the resonance frequency of the disc and the energy dissipation. The frequency shift Δf is related to the mass adsorbed

on the disc surface, described by Sauerbrey equation, $\Delta m = -C\frac{1}{n}\Delta f$, where n denotes different overtones of resonant frequency. The energy dissipation, ΔD, implies the surface rigidity, which offers valuable insights into hydration/cross-linking or conformational change of the surface.

3 Experimental

3.1 Materials

All chemicals were of analytical grade, purchased from Sigma-Aldrich and used without any further purification.

3.1.1 Calcium and Phosphorus Sources

Calcium nitrate tetrahydrate [$Ca(NO_3)_2{\cdot}4H_2O$] and 85 % phosphoric acid (H_3PO_4) were the sources for the preparation of calcium phosphates.

3.1.2 LCP System

The surfactant Pluronic® L64 ($EO_{13}PO_{30}EO_{13}$), H_2O and *p*-xylene were chosen for the formation of LCPs. This system had been studied thoroughly by Alexandridis and co-workers. The ternary phase diagram of this system is shown below:

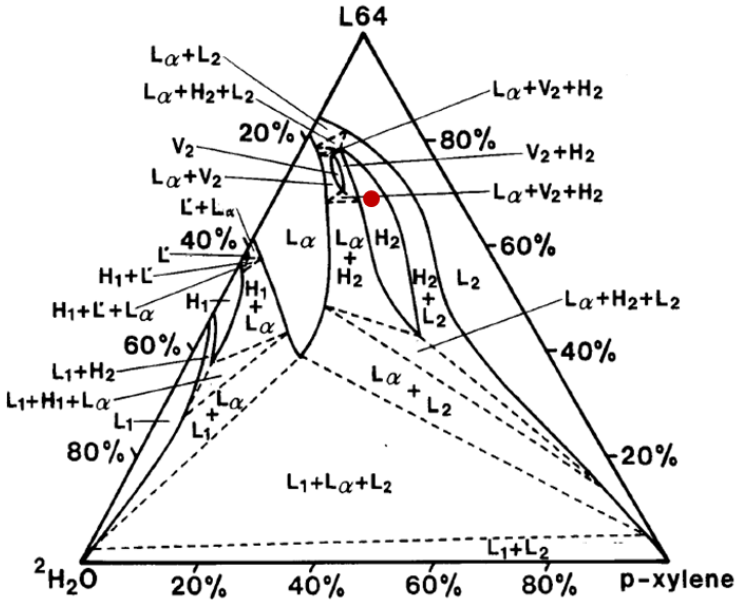

Figure 16: Phase diagram of the L64, H_2O and *p*-xylene system.[48]

The recipe adopted for forming a reverse hexagonal (H_2) phase was 15 wt% aqueous solution, 70 wt% L64 and 15 wt% *p*-xylene marked as a red dot in Fig. 16. Lamellar (L_α) phase with a composition of 35 wt% aqueous solution, 55 wt% L64 and 10 wt% *p*-xylene was also prepared for the inspection of the LCP structure. Additionally, normal hexagonal phase (H_1) was prepared with 50 wt% salt solution and 50 wt% surfactant for studying the influence of initial salt concentration.

3.1.3 GAGs

The GAGs utilised in this project were heparin (sodium salt from porcine intestinal mucosa, Grade I-A, ≥180 USP units/mg) and chondroitin-4-sulfate (sodium salt from bovine trachea). Heparin was chosen because of its relative high density of anionic sites (sulphate groups) and conformational flexibility due to its iduronic acid-rich molecular structure.[53] These two features might render heparin more readily to bind

on HA surfaces. C4S was selected as a representative for glucuronic acid-rich GAGs for the examination of GAGs – HA surface interaction.

3.2 Synthesis

3.2.1 LCP route [54]

$Ca(NO_3)_2 \cdot 4H_2O$ and H_3PO_4 with a Ca:P ratio of 1.67 were dissolved in Milli-Q H_2O at different initial concentrations, (noted as weight percent of $Ca(NO_3)_2 \cdot 4H_2O$ in aqueous solution): 3 wt%, 10 wt%, 20 wt% and 30 wt%.

For the formation of LCPs, the prepared salt solution, Pluronic® L64 and *p*-xylene were evenly mixed. After being equilibrated for 24 hours, the LCP gel was applied onto a clean glass plate (gel thickness ~ 6 mm) and placed in an ammonia atmosphere (ammonium hydroxide, 35 wt% aqueous solution) to increase the pH, thus to initiate the reaction within the water domains. After certain time periods, the reaction was stopped and the obtained material was purified using filtration with water and ethanol alternately for several times. The final product was freeze dried.

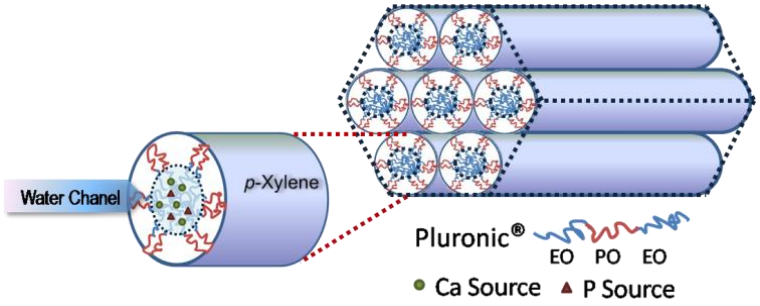

Figure 17: Illustration of the formed H_2 LCP.

3.2.2 WBP route

For the WBP route, the same salt solution was stirred at 500 rpm and directly exposed to an ammonia atmosphere for certain time lengths. The purification process for WBP samples was the same as for the LCP, as described above.

3.2.3 Aging Process

Some of the freshly formed and purified calcium phosphates also underwent an aging process. They were well dispersed in Milli-Q H_2O with or without GAGs and aged at different temperature (room temperature ~ 22° C, 120° C, 200° C and 250° C) for different time lengths. The post-treated particles were filtered, washed with ethanol and freeze dried.

3.3 Examination of LCP Gel Structure

PLM and SAXS were used for identifying the LCP structure.

For the preliminary determination of LCP phase, PLM was conducted on an Olympus polarizing microscope (BH 2-UMA) equipped with DP12 digital microscope camera (magnification 10×). The specimens were prepared by applying a thin layer of LCP

gel on a glass slide and then covered with a coverslip.

The details of the long range orderings in the LCP gel were examined by SAXS. The scattering data were recorded by an MBraun system with an acquisition time of 900s, and the X-ray was generated by a Philips PW1830 X-ray generator. The gel was mounted in a slit (1 mm thick) enclosed by two parallel transparent cellophane films within a stainless steel sample holder.

3.4 Tracking of the Particle Formation Process

TEM was used for investigating the formation and growth of the particles within the LCP structure. After being subjected to NH_3 for certain amount of time, ca 2 ml gel was collected and dissolved in ethanol and centrifuged by a Hettich ALC Centrifuge at 2500 rpm for 10 min. The supernate was removed gently and the sedimentation was re-dissolved in ethanol. This centrifuging-dissolving process was repeated for 4 times and then, the obtained solution was used for preparing TEM specimens.

3.5 Characterization of Synthesized Particles

For the obtained particles, powder XRD, TEM, SEM and BET were utilized to obtain the crystallographic and microstructural information, etc.

To study the crystal structure and crystallinity, the grinded samples were analyzed with a Bruker D8 Advance X-ray diffractometer (Cu-Kα radiation, λ = 1.5418 Å). The sample was scanned from 20° to 60° (2θ) with a scan speed of 2°/min at room temperature.

Sample morphology was investigated by TEM, performed on a JEM-I200EXⅡ microscope (JEOL Ltd.), operated at 120 kV. The TEM specimens were prepared by first dispersing sample powders in ethanol, sonication for 20 min, and then placing a drop of well-dispersed sample solution on a carbon coated copper grid. The specimen was air-dried before characterization.

The topography and chemical compositions of sample 151-A and 153-A were examined using SEM (LEO ULTRA 55FEG), operated at 5 kv.

The specific surface area of as-formed particles was determined by BET nitrogen adsorption, conducted on a Micromeritics Tristar 3000 surface area and porosity analyzer. Approximate 300–500 mg samples were placed in 1/2 inch sample tubes and degassed in a vacuum oven at 120 ℃ for 3 hours before each measurement.

3.6 Detection of GAGs – HA Interaction

The GAGs – HA surface interaction was monitored by QCM-D using a Q-Sense E4 Auto system with four flow modules with which parallel experiments were conducted simultaneously.

Sensor crystals were coated with hydroxyapatite (10 nm Promimic $HA^{NANO™}$ on Ti, QSX 327). The cleaning of the sensor discs before each experiment was done by first

performing a UV-treatment for 10 min, then consequent immersion in 99% ethanol for 30 min, followed by washing with Milli-Q H_2O and thorough blow-drying with N_2 and then a final exposure to UV-light for 10 min.

To determine the adsorption of heparin onto HA, heparin solutions (in Milli-Q H_2O) with different concentrations were prepared, 0.010 wt%, 0.031 wt%, 0.092 wt% and 0.152 wt%. For reproducibility, four identical measurements were carried out in four modules at 23 ℃ for each set of experiment. Heparin solutions with increasing concentrations were passed through the sensors in succession. In between each injection, the frequency and dissipation signal was awaited to be stabilized. All the experiments were started and ended by rinsing with Milli-Q H_2O.

The study of adsorption behavior of C4S was conducted at concentrations of 0.010 wt%, 0.030 wt%, 0.090 wt% and 0.152 wt%.

3.7 Complementary Analysis

To complement the comparing characterizations of LCP and WBP samples, several other techniques were involved in this project.

TGA and TGA-IR were carried out by Christopher S. Knee from Dept. Chemistry, Gothenburg University. The TGA measurements were operated from room temperature to 850^{o} C at a rate of 10 ℃/min.

Raman spectroscopy was conducted by Johan Bielecki from Dept. Applied Physics, Chalmers University of Technology.

Synchrotron radiation SAXS was performed by Martin Andersson (Dept. Chemical and Biological Engineering, Chalmers) at MAX-Lab beam station 7-11, Lund. The H_2 gel was prepared using the same method and recipe as described earlier, with a salt concentration of 10 wt%. The synchrotron SAXS was done on gel before (stayed in NH_3 for 0 hours) and after (stayed in NH_3 for 72 hours) the reaction.

4 Results

4.1 LCP Gel Formation

The formed H_2 gels with a composition of 15 wt% salt solution, 70 wt% L64 and 15 wt% *p*-xylene were transparent, birefringent and highly viscous. While the L_α gels prepared by mixing 35 wt% salt solution, 55 wt% L64 and 10 wt% *p*-xylene were transparent, birefringent and had certain flowability.

4.1.1 LCP Structure

The anisotropicity of the prepared H_2 and L_α gels were preliminarily investigated by PLM (Fig. 18). The angular texture and striations shown in (a) and (b) are rather typical for hexagonal structure, whereas the fan-like units with a black cross at the center (c) and mosaic patterns (d) can be proof for the existance of lamellar phase.

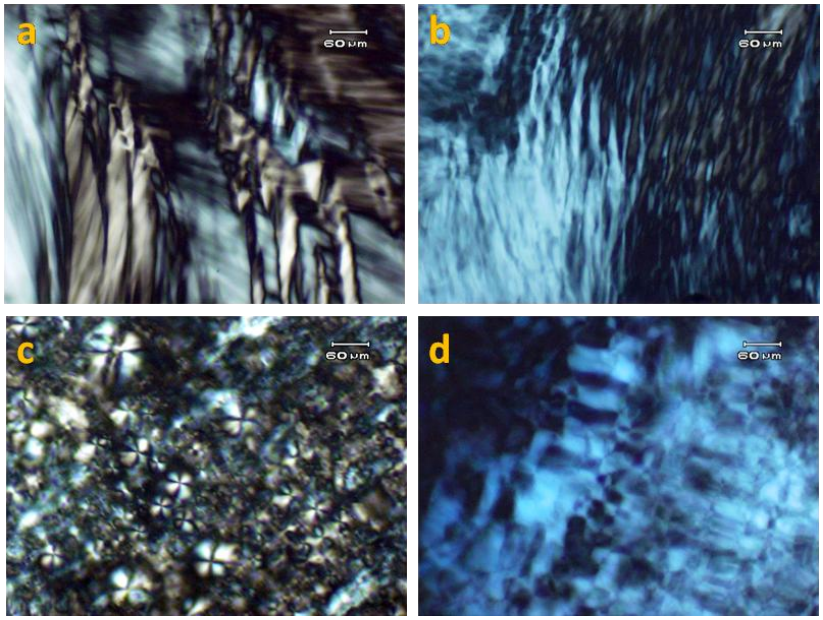

Figure 18: PLM images of prepared H_2 (a, b) and L_α (c, d) gel.

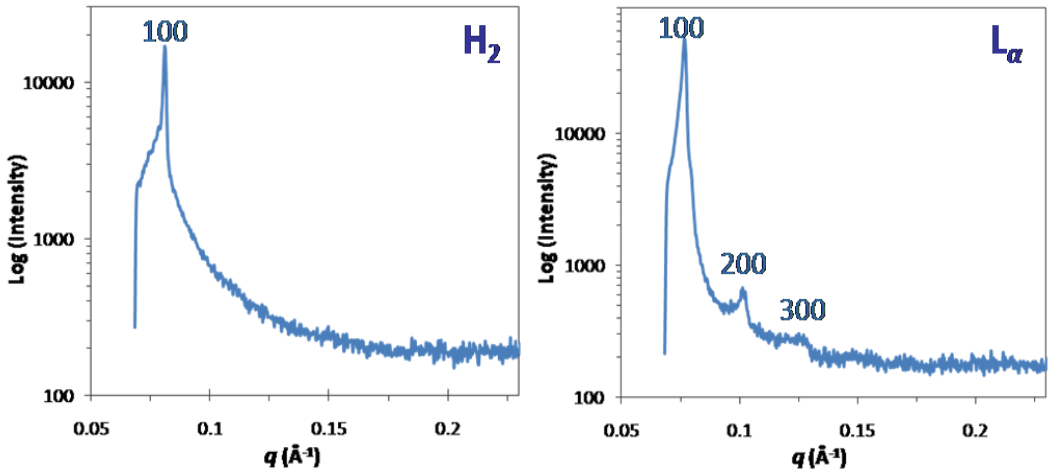

Figure 19: SAXS patterns of prepared LCPs.

Since direct observation cannot provide specific phase information, SAXS was further used in identifying the LCP structure. For H_2 phase, the single peak (Fig. 19, left) merely suggests the long-range order of this system. The absence of other peaks may be due to the imperfection of formed LCP structures or the less sensitivity of X-ray lab source. While for L_a phase, the reflections obeying the 1:2:3 relationship (three peaks' position in Fig. 19, right) indicate the formed one-dimensional lamellar structure.

From synchrotron SAXS spectra (Fig. 20), the obvious reflections submitting to the relationship $1:3^{1/2}:2$ can be observed, which confirm the hexagonal structure of the gel before (left) and after (right) stayed in NH_3 atmosphere. The slope presented before the first-order peak (the right spectrum) can be attributed to the formation of solid particles, since the gel had been stayed in NH_3 for 72 hours before the characterization. These results prove that the H_2 structure was maintained during the whole particle formation process.

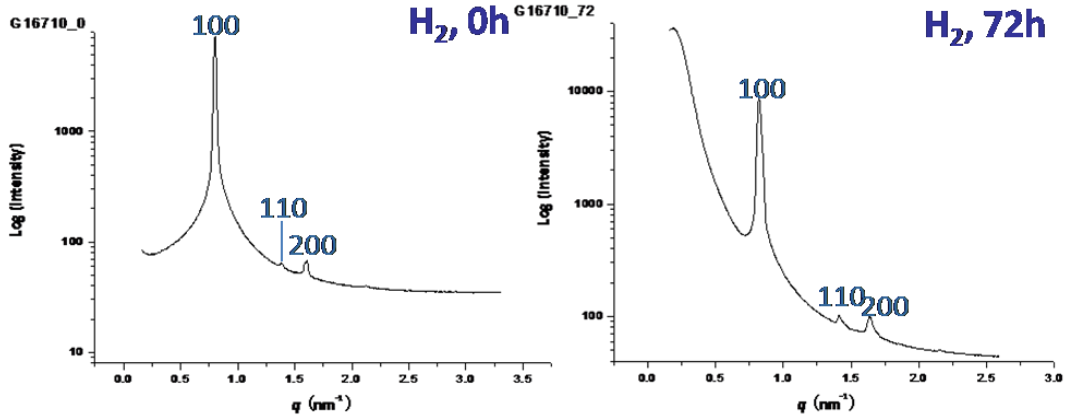

Figure 20: Synchrotron radiation SAXS spectra of H_2 gel with 10 wt% salt conc. before and after reaction, by M. Andersson.

Table 2: Lattice parameter of LCP phase calculated from Fig. 20.

Reverse Hexagonal Phase							
h	k	n	d_{hex} (Å) from ref. 48	q_{obs} ($Å^{-1}$) 0 h in NH_3	d_{hex} (Å) 0 h	q_{obs} ($Å^{-1}$) 72 h in NH_3	d_{hex} (Å) 72 h
1	0	1	92	0.080	90.35	0.082	88.48
1	1	3		0.139	90.41	0.141	89.12
2	0	4		0.160	90.58	0.165	88.21

$n=h^2+hk+k^2$, $q_n=4\pi/d_{hex}$

Furthermore, the lattice parameter d_{hex}, i.e. the distance between two adjacent cylindrical domains was calculated from the peak position q_{obs} in Fig.20, and is shown in table 2. With the volume fraction Φ_{cyl}, the cross section radius of water channels R_{cyl} can be obtained by,

$$R_{cyl} = d_{hex}[(3^{1/2}/2\pi)\,\Phi_{cyl}]^{1/2}.$$

With the calculated data, a schematic cross-section of the cylindrical domains of the as-formed H_2 phase can be obtained as is shown in Fig. 21. These water domains with a diameter of approximately 6 nm were the locations where the particle formation took place.

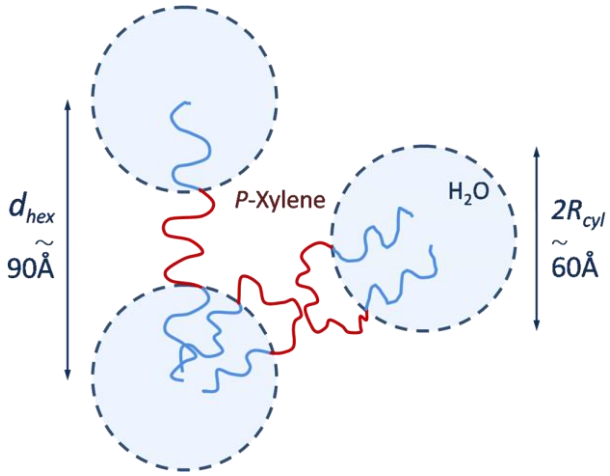

Figure 21: Illustration of obtained H_2 phase.[48]

4.1.2 LCP Stabilizing Time

Additionally, the possible influence of LCP stabilizing time before putting into NH_3 atmosphere was also examined by SAXS (Fig. 22). No obvious difference was observed, which suggests that the H_2 gel structure was well preserved before initiating the reaction.

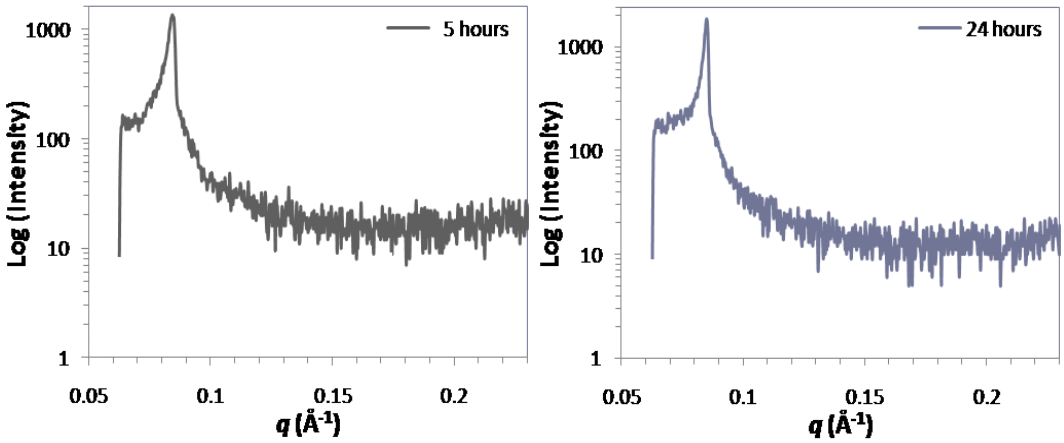

Figure 22: SAXS patterns of LCP stabilized for 5 and 24 hours.

4.2 Particle Formation Process in LCPs

The particle formation process was triggered by the diffusion of NH_3 into the LCP structure. It took 2 – 3 days for NH_3 to completely penetrate into the whole gel layer (~ 6 mm) and the resulting pH was 10 – 11. The formed particles were amorphous, which could be confirmed by the characteristic halo peaks that appeared in the XRD patterns (Fig. 23). Never the less, there might be certain local atomic ordering of the attained ACPs as researchers have claimed that ACP could be composed of the Posner's clusters $[Ca_9(PO_4)_6]$ with a dimension of 9.5 Å. These cluster units may be

further packed hexagonally to form hydroxyapatite.[31, 32]

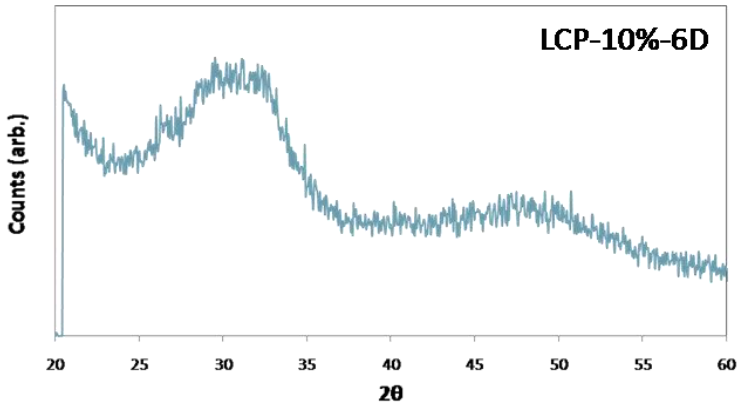

Figure 23: XRD pattern of the particles formed in LCP structure.

4.2.1 Initial Salt Concentration

The influence of the initial salt concentration in the water domains on the morphology of formed particles was examined. Although LCPs consisting of Pluronic are known to have low sensitivity to the addition of salts (little effect on CPP), different salt concentration will affect the volume fraction of the system and could also play a significant role in the particle formation behavior inside the confined nanometric domains.

Fig. 24 shows the comparison between ACPs prepared with 3 wt% and 10 wt% salt solution. The specific surface areas of the particles were in the range of 150 – 174 m^2/g (left). The performance of the 3 wt% salt solution might be slightly better than that of 10 wt%. While from the TEM micrographs (right), the ACPs obtained by both concentrations are all spherical particles with diameters of 8 – 12 nm. The electron-lucent centers of ACP spherules were probably caused by electron beam damage.[55]

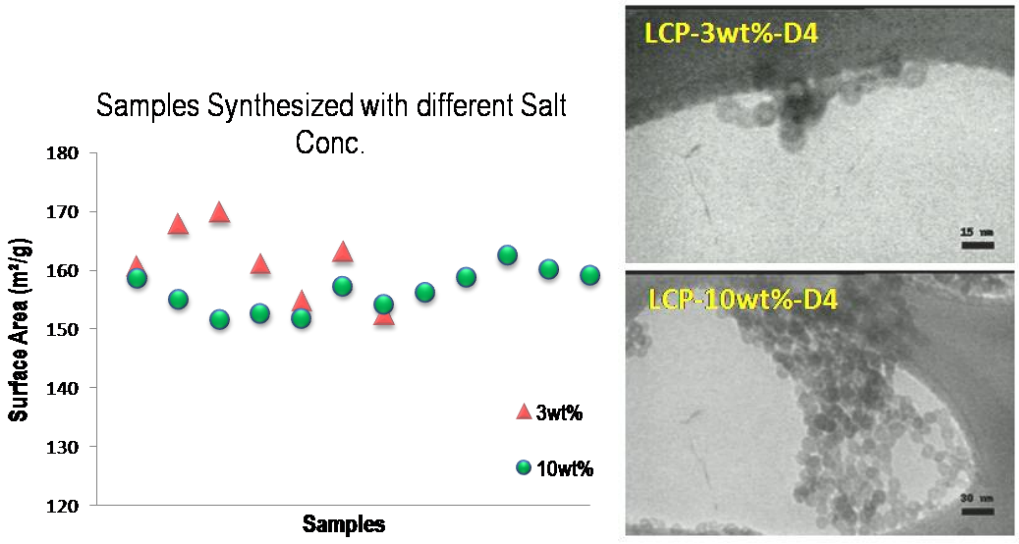

Figure 24: BET and TEM results for particles prepared with 3 wt%, 10 wt% salt conc..

When increasing the initial salt concentration to 20 wt% or even 30 wt%, different

scenarios were presented (Fig. 25). The particles formed within 2 days for both concentrations were a mixture of ACP spherules and long rod arrays with a thickness of roughly 6 nm. The possible reason for this discrepancy caused by different salt concentrations will be explained in the discussion section.

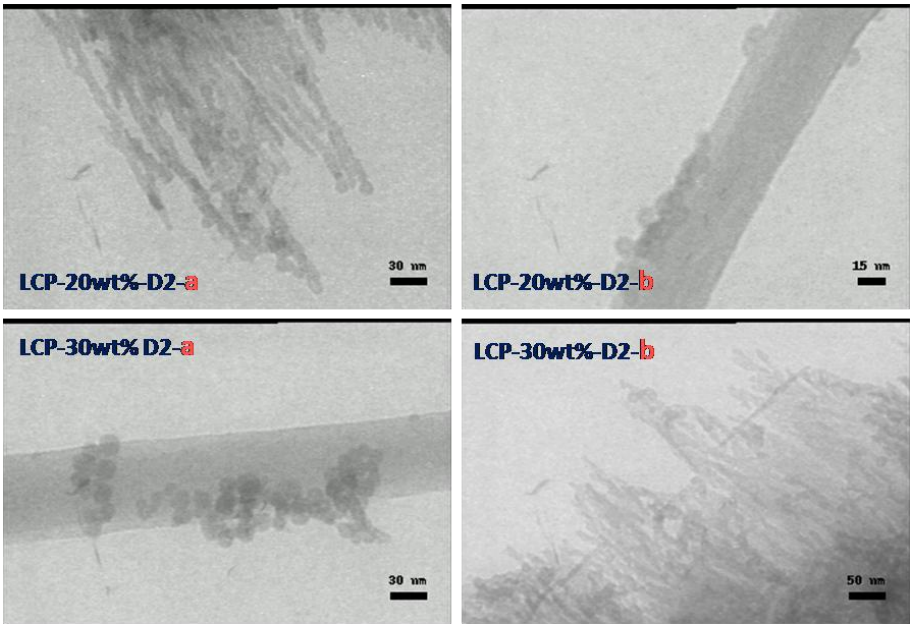

Figure 25: TEM images of ACPs obtained with 20 wt% and 30 wt% salt conc..

Fig. 26 shows the particles synthesized using the H_1 phase with 30 wt% salt solution. Since the water domain is continuous in this case, there is less restriction during the particle formation process. Therefore, the broad distribution of particles' size (from microns to nanometers) is quite reasonable (left image). In addition, the coexistence of large electron-dense ACPs and spherical clusters of rod-like crystals with more or less the same size was observed as well (right). Hence, it can be postulated that the conversion of ACP to HA occurred in-situ. The occurrence of big crystals in H_1 gel that lingered in NH_3 only for two days also suggests the inferior stability of this system.

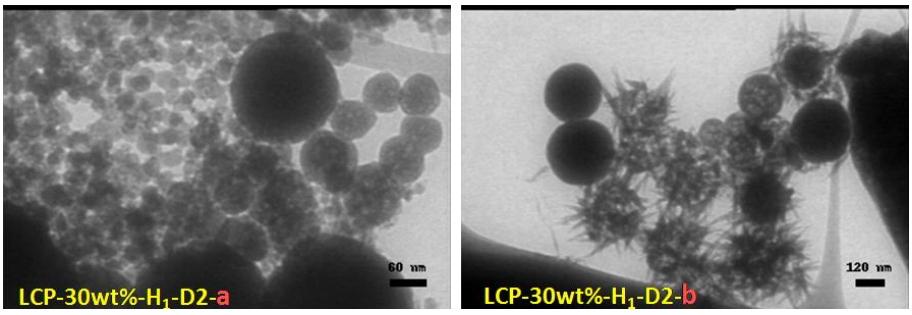

Figure 26: TEM images of particles synthesized by H_1 gel with 30 wt% salt solution.

4.2.2 Linger Time in NH_3

TEM was utilized to follow the particle formation process in the LCP structure. Fig. 27 shows the particles formed in the H_2 gel after being subjected to NH_3 for 1 – 8 days (prepared with 10 wt% salt solution). Basically, the ACP spherules were fairly

stable in this system. After the first two days, there was a disparity in ACP particle diameters (from 2 to 10 nm), which probably was due to the pH gradient caused by the slow diffusion of NH_3. After 2 days in NH_3, the size of ACP spherules became more evenly distributed, with diameters of 8 – 12 nm.

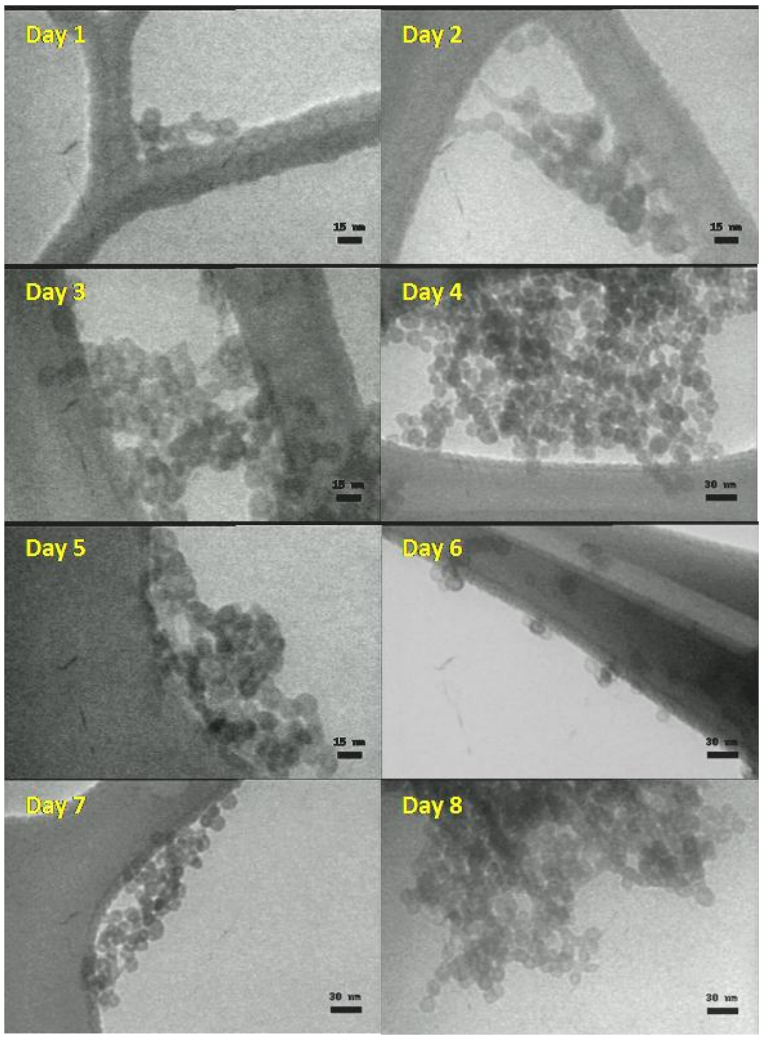

Figure 27: TEM micrographs of ACP spherules stayed in NH_3 atmosphere for 1-8 days (10 wt% salt conc.).

When prolonging the stay in NH_3 atmosphere to 26 days, plate-like HA crystals other than ACP spherules were also present (Fig. 28). This case indicates the destruction of certain parts of the LCP structure, where the ACPs were directly exposed to NH_3, and quickly converted to big crystals without any restriction.

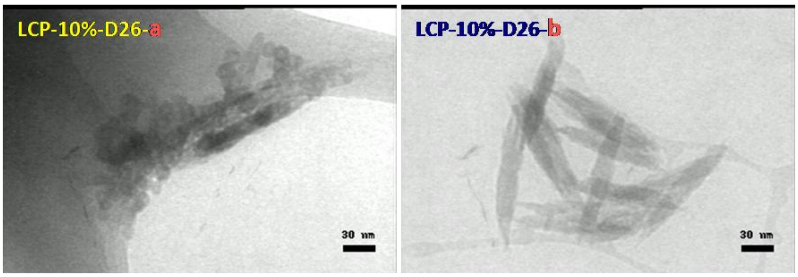

Figure 28: TEM images of particles stayed in NH_3 for 26 days (10 wt% salt conc.).

For relatively high initial salt concentrations 20 wt% and 30 wt%, the H_2 systems were far less stable. The particles formed in the LCP at day 3 were still a mixture of amorphous long rod arrays and spherules (Fig. 29, top). However at day 4, HA crystallites started to emerge for 20 wt% salt solution (Fig. 29, bottom right), which implies the loss of H_2 structure.

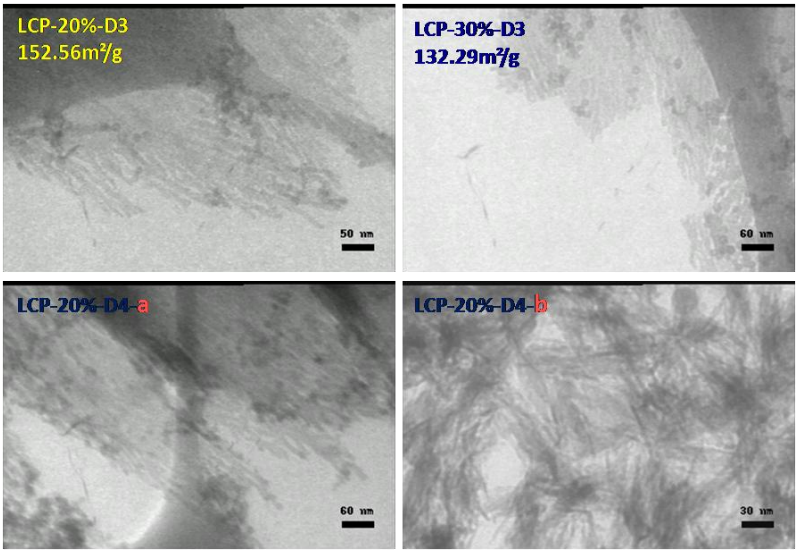

Figure 29: TEM micrographs of ACP rod arrays lingered in NH_3 for 3 and 4 days with initial salt conc. 20 wt% and 30 wt%.

4.3 Aging Process

4.3.1 Termination of ACP – HA Conversion

As we know, the freshly formed ACPs will gradually convert to HA in water media. Therefore, knowing how to stop the conversion is of great importance in controlling the morphology of the obtained particles.

Fig. 30 shows the comparison between particles final-washed by ethanol and water. For the sample final-washed by ethanol, spherical ACP structure was retained (TEM image, upper-left) and the specific surface area was ranging from 150 to 170 m^2/g. On the other hand, the sample final-washed by water was plate-like crystals (sample no. 114, TEM image, middle-left) with specific surface areas mostly lower than 120 m^2/g. Contrarily, the same sample (no. 114) in LCP (TEM, bottom-left) and right after purification (TEM, bottom-right) was still spherical ACP particles. Hence, the crystallization of samples final-washed by water happened during aging as a result of the residual water moiety. In addition, for the sample first aged in water for 19 hours, then final-washed by ethanol (TEM, upper-right), the occurrence of newly converted needle-like crystallites with high aspect ratio increased its specific surface area to nearly 200 m^2/g (blue circle in left diagram). Sample no. 63 was final-washed by water, but then put into vacuum oven after certain time length's aging. Interestingly, the particles were all converted to and locked at the needle-like crystallite state (TEM, middle-right) and the specific surface area was around 200 m^2/g.

Consequently, the extraction of water from particles is the essence for the termination

of ACP – HA conversion, which can be achieved using ethanol washing, vacuum oven or freeze-drying.

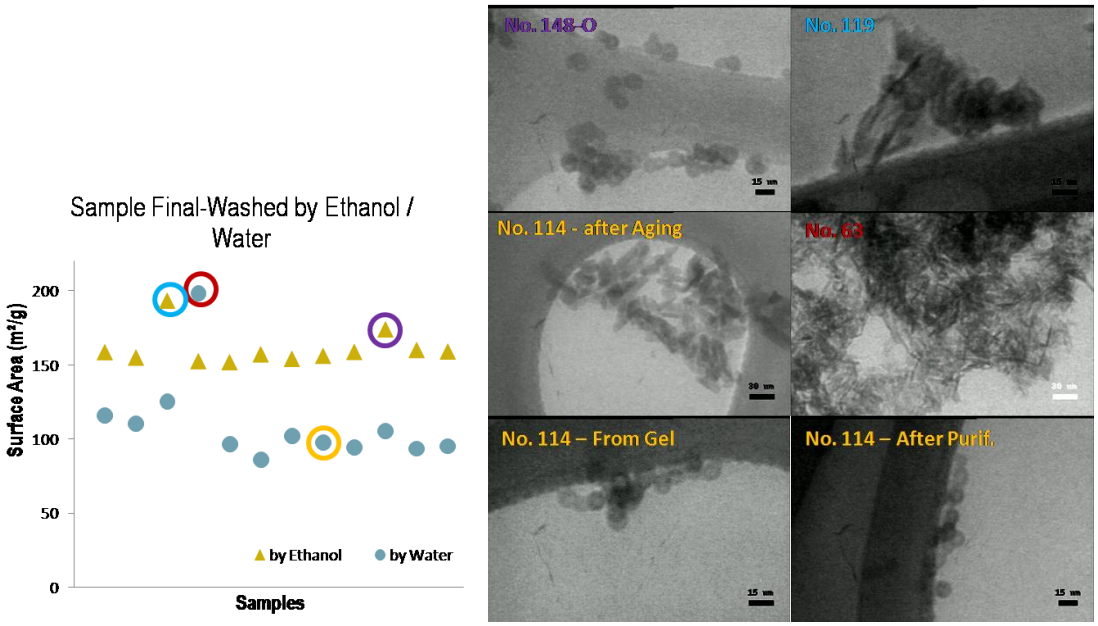

Figure 30: BET and TEM results for particles final-washed by ethanol/water.

4.3.2 Aging at Room Temperature

A controlled ACP – HA conversion was proceeded at room temperature (~ 22° C).

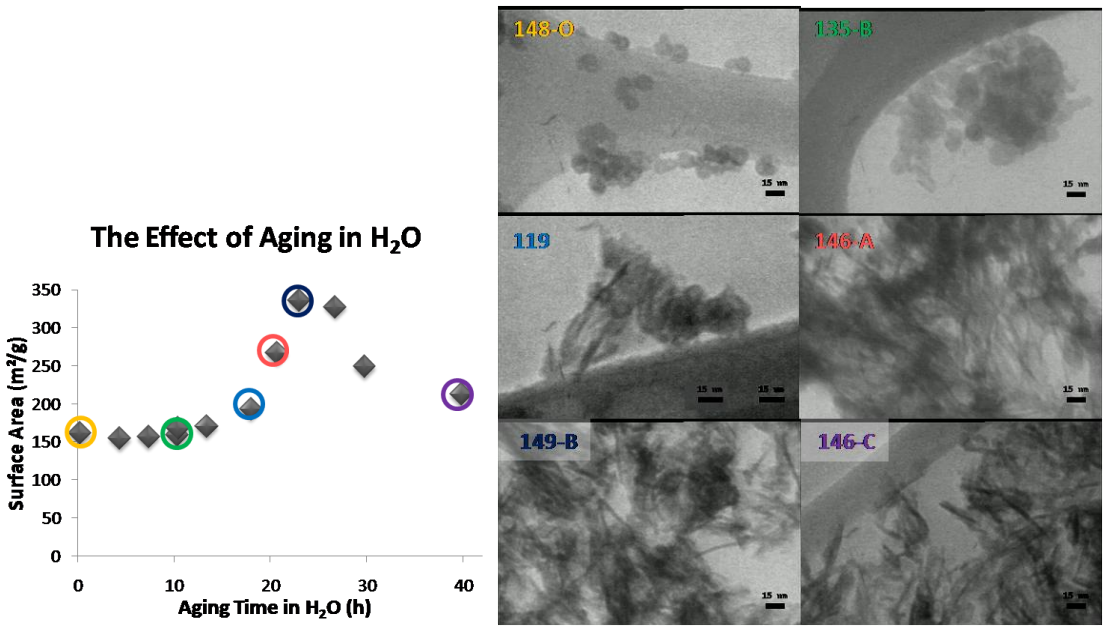

Figure 31: BET and TEM results for particles aging in water for different hours.

An apparent trend in the specific surface area could be observed when the particles were aged at different times (Fig. 31, left). For the first 16 hours, the specific surface area of the particles was maintained at around 160 m^2/g. While seen from the TEM (upper images), the ACP spherules became diffused and dissolved during this stage. When aged for 16 to 25 hours, the crystallites with high aspect ratio started to form (TEM, middle-left), which led to a drastic increment in specific surface area. When

aged for 24 hours, the majority of ACPs had converted to needle-like crystallites (TEM, bottom-left) and the surface area almost reached 340 m^2/g. After 26 hours, the converted crystallites grew further (especially in width, see TEM bottom-right) into platelets, resulting in a drop in specific surface area.

Thus, the ACP – HA conversion at room temperature can be divided into three stages, induction period (~ 0 – 16 h), crystallization (~ 16 – 26 h) and crystal growth (> 26 h).

4.3.3 Aging under Heat

Fig. 32 shows the aging behavior of particles under heat. When aged at 120 ℃ for 7 min (upper-left), no crystallization occurred, ACPs were still at induction period and the large size distribution of ACP spherules was attributed to the Ostwald ripening. When increasing the temperature to 200 ℃, ACPs transformed to HA within 2 min (upper-middle). While for 250 ℃, 1 min was enough for ACPs' crystallization (bottom-left). Accordingly, the higher the temperature, the faster ACP converts. However, since the conversion period is quite short, there is less controllability in products' morphology at high temperatures.

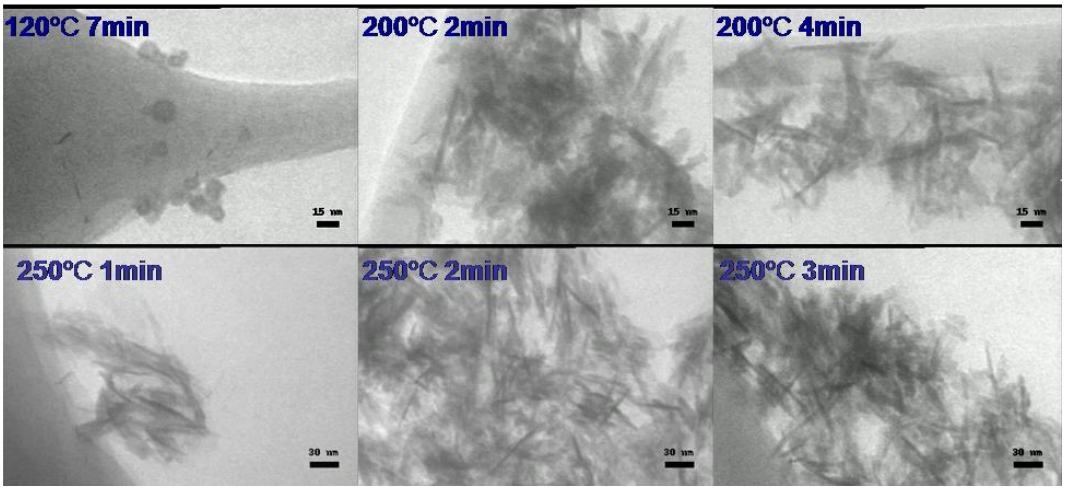

Figure 32: TEM images of particles aging at high temperature.

4.3.4 ACP – HA Conversion

The XRD diffractograms of particles lieing in distinct converting stages are presented in Fig. 33 (left). From bottom to top, the conversion started from ACP with broad halos in the XRD pattern and followed by the transient precursor stage indicated by the exceptive peaks (pointed by arrows), which belonged to brushite. The subsequent phase was the poorly crystallized apatite (PCA) with broad and diffused peaks that shared the basic shape of the HA structure. The PCA further crystallized into HA, accompanying the sharpening and refinement of the XRD peaks.

Fig. 33 (right) shows the sample from the same batch that aged in water for 20, 30 and 40 hours. The narrowing and sharpening of HA peaks with increased aging time can be clearly observed.

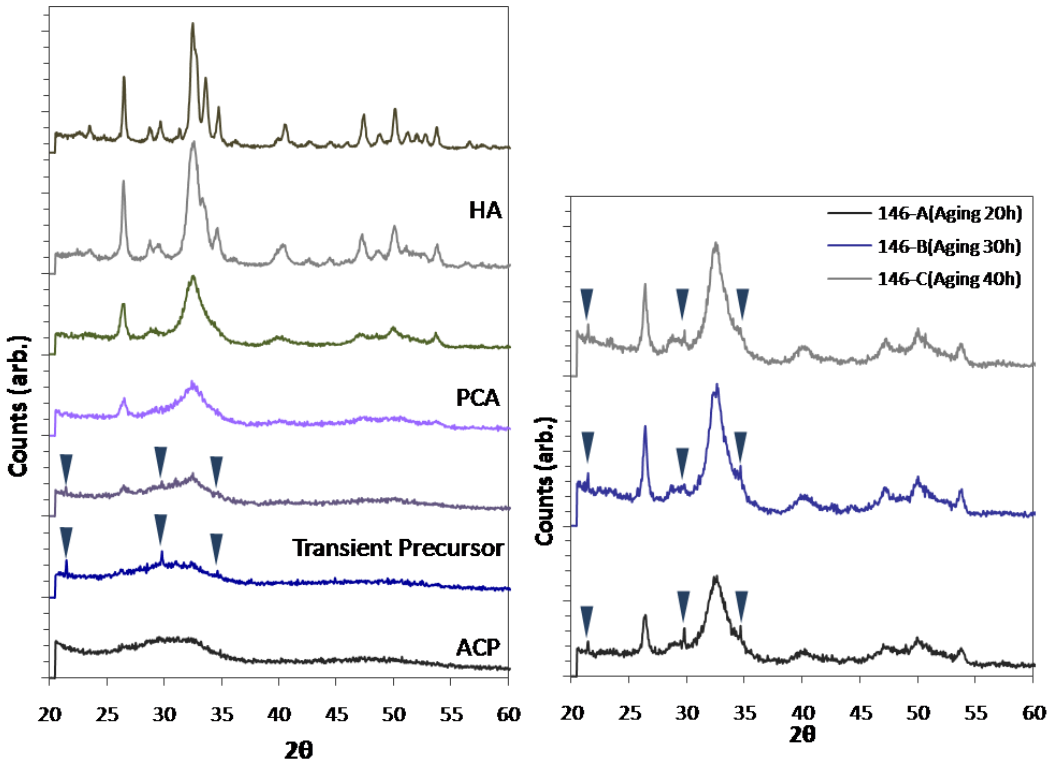

Figure 33: XRD patterns of particles at different conversion stage.

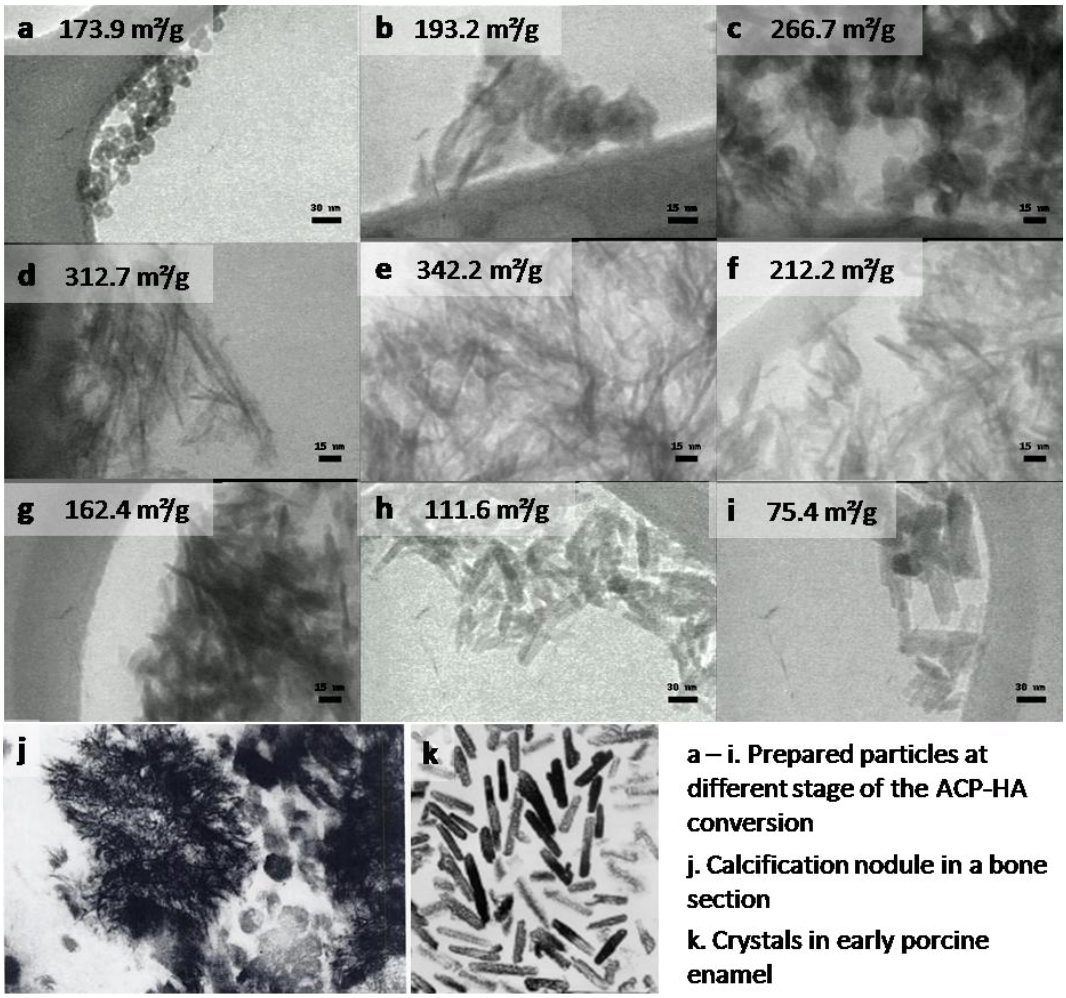

Figure 34: TEM micrographs of particles at different conversion stage.[28, 57]

Fig. 34 shows the morphological changes of particles during the ACP – HA conversion. It starts from the ACP spherules with diameter 8 – 12 nm (a), followed by the appearance of needle-like crystallites (b). Then comes the coexistence of diffused ACPs and crystallites (c), and consequent crystallization of residual ACPs (d, e). The further growth in crystallite width can be seen in (f, g) and the final transformation to big HA platelets is referred to (h, i). The coexistence of electron-dense ACPs and needle-like crystallites was also observed in bone nodule (j), which was at the early stage of the ACP – HA conversion. While the rod-like HA crystals found in enamel (k) suggested the progress in the latter stage to be crystal growth.

4.4 Addition of GAGs

4.4.1 GAGs – HA Interaction

The GAGs – HA surface interaction was examined by QCM-D. Two sets of monitoring were conducted at 23 ℃ (Fig. 35: with heparin, Fig. 36: with C4S). Signals from overtones 3 – 13 and 3 – 9 were collected. The steps shown in the frequency and dissipation curves correspond to each injection of GAGs solution with an increased concentration.

The frequency in Fig. 35 showed an obvious drift. The Δf in both cases were rather small compared to a real adsorption, which suggests that the GAGs – HA interaction is quite weak. Increases in absolute value of Δf and ΔD were still observed with increasing GAGs concentration. However, this change cannot be a definite proof for the adsorption process, since it may probably be caused by the increase in viscosity of the injected solution. The great disparity in dissipation signal strength of the different overtones indicates that the "adsorbed" layers are rather soft, implying the flexibility of GAG molecules on HA surface.

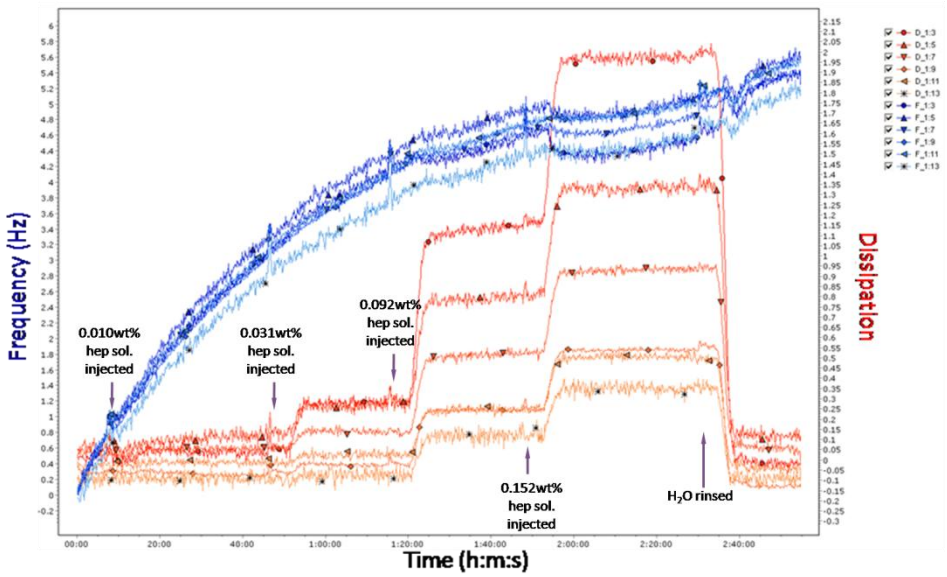

Figure 35: Adsorption of heparin onto HA-disc at 23 ℃. Four steps correspond to the injection of heparin solution with conc. 0.010 wt%, 0.031 wt%, 0.092 wt% and 0.152 wt%, respectively. Experiments were started and ended by rinsing with Milli-Q H_2O.

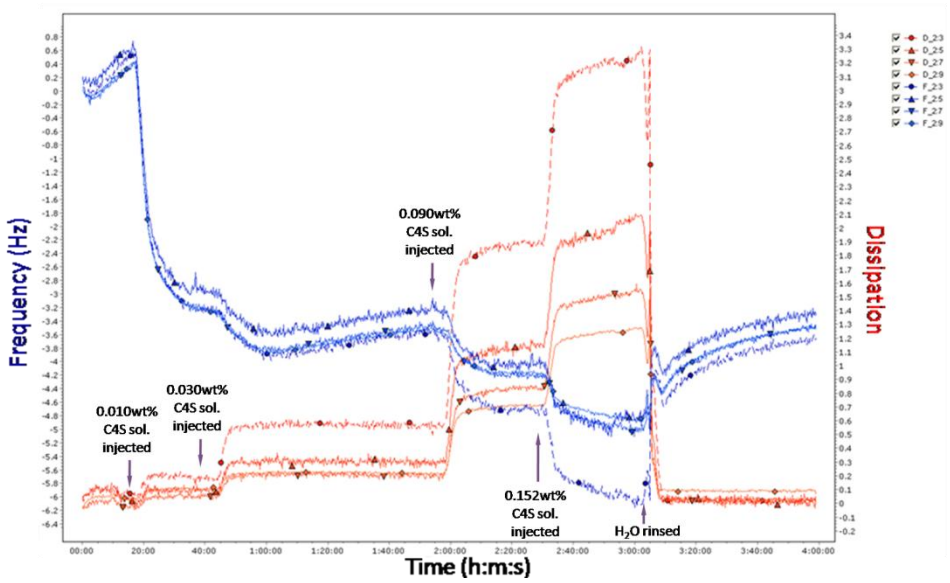

Figure 36: The adsorption of C4S onto HA-disc at 23 ℃. Four steps correspond to the injection of C4S solution with conc. 0.010 wt%, 0.030 wt%, 0.090 wt% and 0.152 wt%, respectively. Experiments were started and ended by rinsing with Milli-Q H_2O.

4.4.2 GAGs' Effect

The aging behavior of ACPs with the existence of heparin (conc. 0.325mg/ml) was examined.

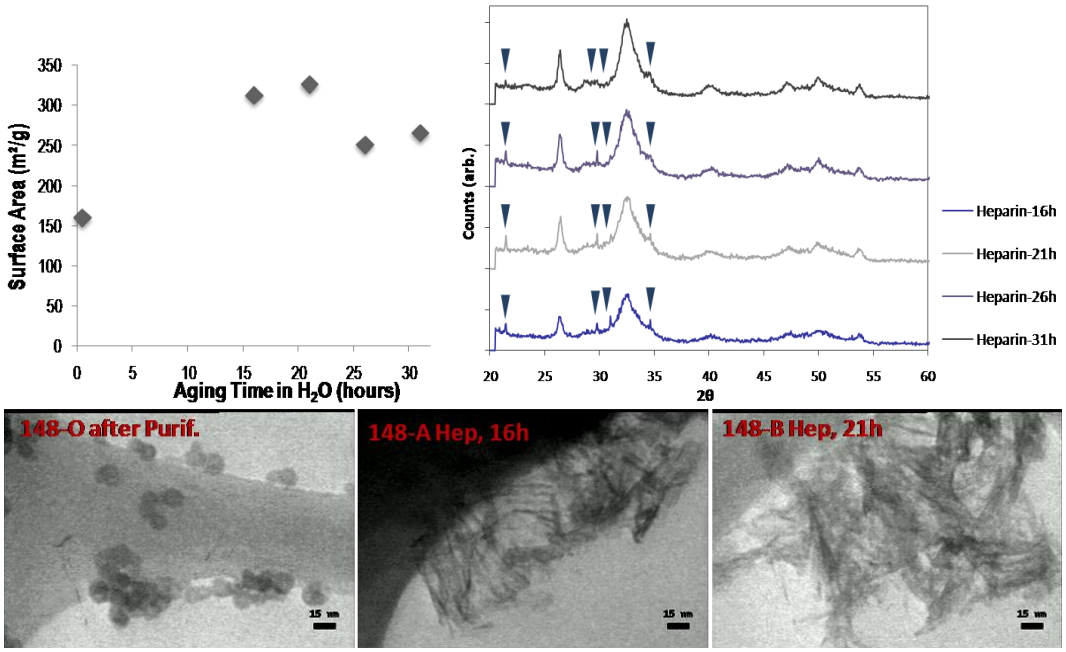

Figure 37: BET, XRD and TEM results for particles aged with heparin (0.325mg/ml).

The first increase followed by the decrease tendency in specific surface area (Fig. 37, upper-left) was more or less the same as for particles aged without the presence of GAGs (Fig. 31, left). The narrowing of the XRD peaks when prolonging the aging time (Fig. 37, upper-right) was observed and the peaks (arrows) indicating that the transient precursor, brushite also was present. In the TEM micrographs (Fig. 37, bottom), the ACP spherules before aging, the coexistence of ACPs and newly formed

crystallites, as well as the clusters of HA crystallites are shown, which displays the different conversion stages.

ACPs originating from the same batch were aged with and without heparin. With the existence of heparin (0.429 mg/ml), large amount of diffused ACPs (dashed circle) were still remained after aging for 23.5 h, whereas the samples that aged for 23 h without GAGs were mostly converted to crystallites (Fig. 38, right). The relatively vague XRD peaks (Fig. 38, left) of heparin-sample compared to the no-GAG-sample, also shows the large amount of amorphous moiety and poorer crystallinity. The subtle vantage in aging time for the heparin-sample, yet with an apparent retardation in conversion stage, suggests the interference of heparin molecules during ACPs' crystallization.

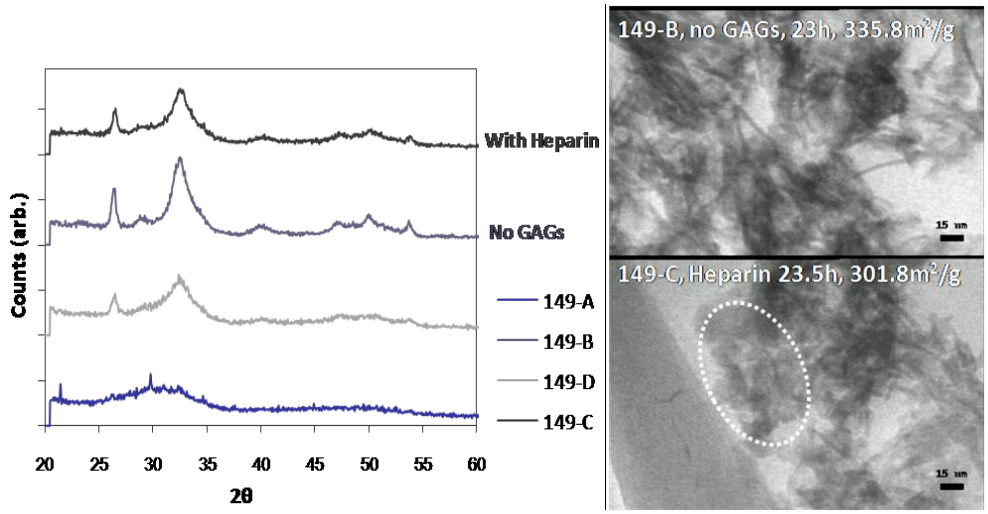

Figure 38: The hindrance of GAGs on ACP – HA conversion (0.429 mg/ml for 149-C).

However, with a longer aging time, heparin-sample could also reach the state where all the ACPs had converted to needle-like crystallites (Fig. 39, middle, right), which attained an extremely high specific surface area, 347.72 m^2/g. Furthermore, from the average atomic percentage information obtained by SEM-EDS (sample 151-A: O 65.02%, Ca 20.77%, P 13.78%, S 0.43%), the Ca/P is calculated to be 1.507, which means the prepared crystallites are calcium deficient. Note that the presented sulfur is brought by heparin.

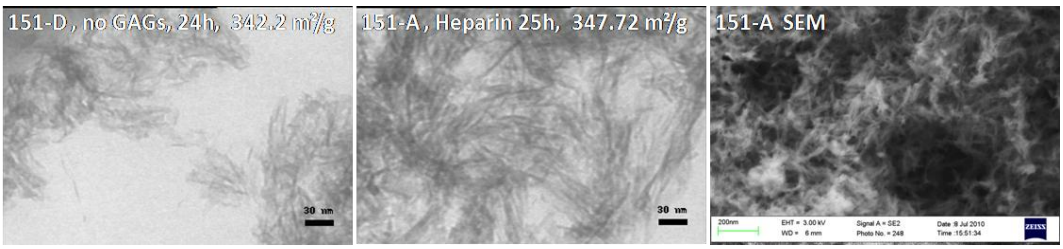

Figure 39: EM comparison of PCAs aged with/without GAGs (0.257 mg/ml for 151-A).

4.5 Comparison between LCP and WBP

Information of samples prepared using LCP and WBP route with and without GAGs is presented in Table 3. Fig. 40 shows HA particles synthesized using the LCP (A and

B), which are needle-like crystallites (about 5×35 nm in size) and by WBP (C and D), which are more plate-like (width ~15 nm). The addition of GAGs increased the specific surface area in both routes, suggesting its interaction with HA.

Table 3: Sample information and BET results.

Sample No.	Synthetic Route	GAGs Conc.	BET Surface Area (m^2/g)
A	LCP	0	218.9
B	LCP	1.54 wt%	277.9
C	WBP	0	75.9
D	WBP	1.54 wt%	85.2

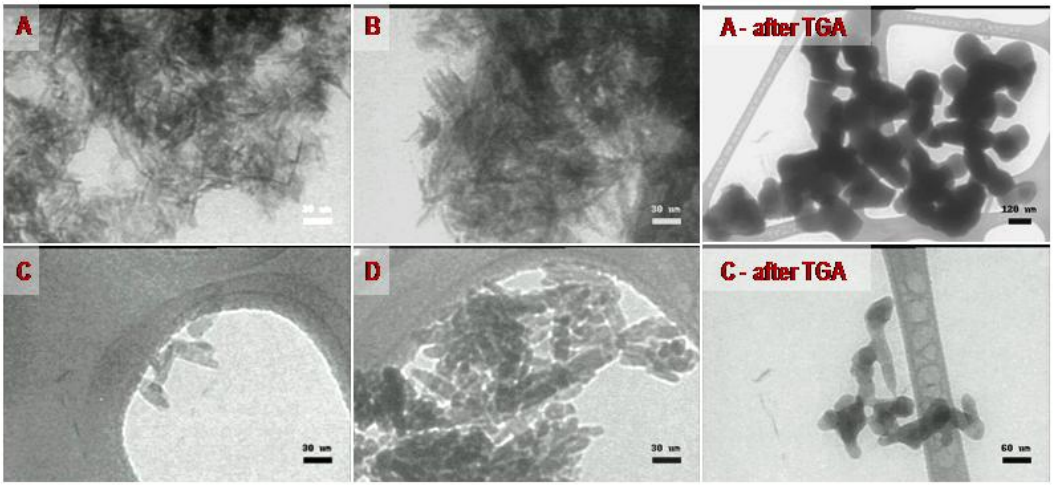

Figure 40: TEM micrographs of LCP and WBP samples before and after TGA.

The thermostability of these samples was investigated by TGA and DSC and the results are presented in Fig. 41.

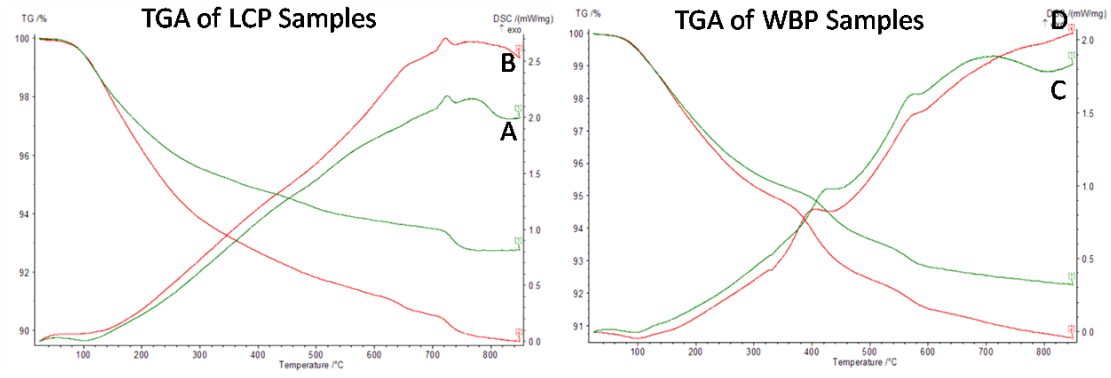

Figure 41: TGA/DSC of LCP and WBP samples, by C. S. Knee.

The TGA curves can be divided in three mass loss stages. The first mass loss observed between room temperature and 250 ℃ is 3.87 %, 5.19 %, 3.65 % and 3.95 % for sample A – D respectively, which corresponds to the loss of water adsorbed on the nano-crystals and the water associated with non-apatite environment. The second stage observed between 250 ℃ and 550 ℃ corresponds to the loss of strongly linked intracrystalline water and the dehydration of HPO_4^{2-} ions,

$2HPO_4^{2-} \longrightarrow P_2O_7^{4-} + H_2O$,

where the HPO_4^{2-} ion originate from the hydrolysis of PO_4^{3-} ion, as a key step for initiating the ACP – HA conversion. The exothermic peaks appearing at around 400 ℃ for WBP samples can be attributed to this condensation.

For HA synthesized by LCP, the third mass loss occurs between 650 ℃ and 850 ℃, corresponding to the reaction of $P_2O_7^{4-}$ and OH^- ions of the apatite structure, forming TCP (bulky electron-dense particles as seen in Fig. 40, upper-right). The exothermic peaks of sample (A) and (B) at around 720 ℃ indicate this transition. While the third stage for the WBP samples occurs between 550 ℃ and 700 ℃, corresponding to the crystallization of ACP moiety (exo-peaks at 570 ℃) and HA crystal growth (bigger size in Fig. 40, bottom-right).

Note that the difference in values of the mass loss between 250 ℃ and 850 ℃ for samples synthesized by the same route with and without GAGs is around 1.54%, which implies the existence of GAGs to some extent (D-value: 1.80 % for LCP samples, 1.33 % for WBP samples).

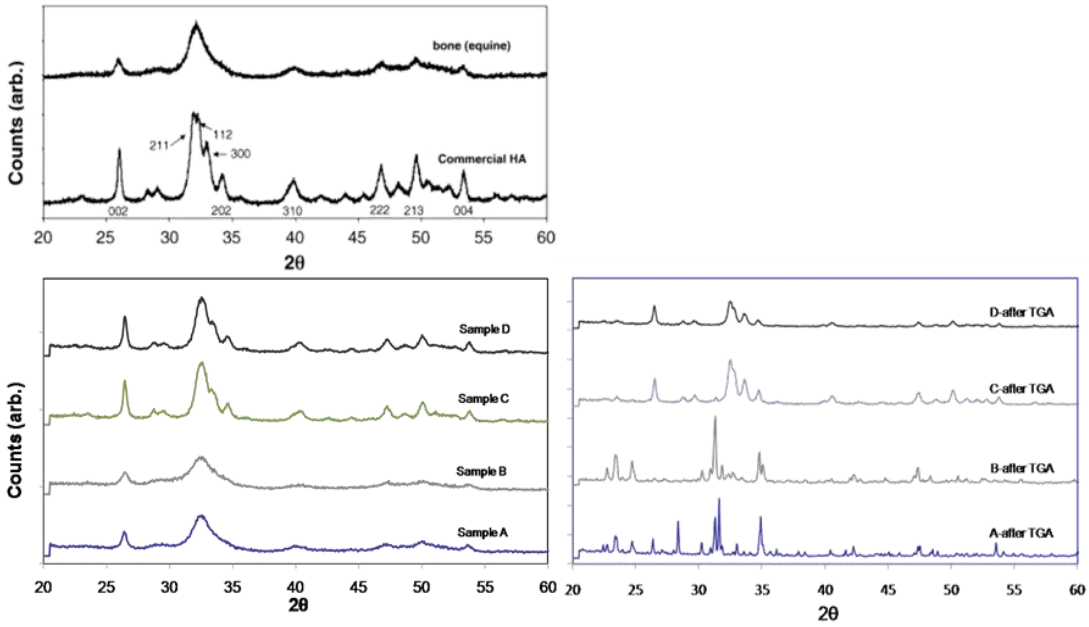

Figure 42: XRD patterns of LCP and WBP samples before and after TGA, compared with bone and commercial HA.[10]

The XRD patterns of samples before and after TGA are shown in Fig. 42. It can be seen that all the samples are of HA structure before the TGA analysis (bottom-left). Additionally, the broad diffuse peaks of LCP samples (A) and (B) indicate that they are poorly crystalline and extremely small in crystallite dimensions, which yielding high specific surface area and inferior thermostability as compared to the WBP samples. While after TGA (all the samples were heated up to 850 ℃), the HA peaks for sample (C) and (D) are much sharpened and refined, indicating that HA are better crystallized and increased in crystallite size. However, for sample (A) and (B) after TGA, the peaks attributed to HA are vanished and peaks identified to be TCP are present. These results

correlates well with observations made by the TGA/DSC, that is, the exothermic peak observed at around 720 ℃ indicate this transition from HA to TCP.

In addition, the XRD patterns of LCP samples have great resemblance to natural bone, whereas those of WBP samples were more close to commercial HA (Fig. 42, upper).

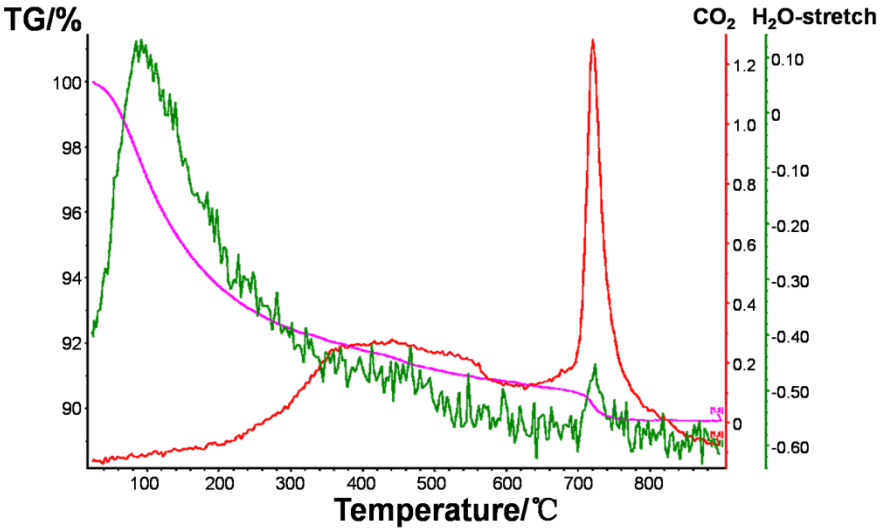

Figure 43: TGA-IR of LCP sample B (with GAGs), by C. S. Knee.

Fig. 43 shows the TGA-IR of sample B, where the pink curve is the mass loss, green line is H_2O stretch intensity and the IR signal for CO_2 is in red. The H_2O stretch peak at ~100 ℃ consolidates our previous analysis that the mass loss below 250 ℃ was attributed to the loss of adsorbed water. Besides, the HA – TCP conversion at around 730 ℃ for LCP sample B, is linked to the new signal of H_2O and CO_2 at ~730 ℃. The strong CO_2 signal shown here indicates that sample B was carbonated HA.

5 Discussion

5.1 ACPs' Formation in LCP Structure

Since the H_2 phase was maintained during the particle formation process, as shown by the synchrotron SAXS results, ACPs' formation took place in the confined H_2 water domain with the diameter of ~ 6 nm, which is illustrated in Fig. 44. The penetration of NH_3 increases the pH in the water domain resulting in that calcium and phosphorus sources react and form amorphous spherules, which will grow further during the reaction process.

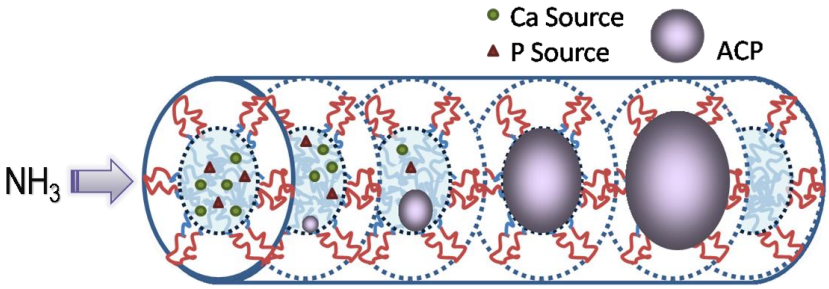

Figure 44: Schematic diagram of ACPs' formation in H_2 structure.

For low initial salt concentration (≤ 10 wt%), the formed ACP spherules have little possibility to interfere with each others' growth. When the individual ACPs reach the border of the water channel, the growth does not cease to continue. They further "squeeze" into the surfactant wall and swell the structure, yielding a diameter of 8 – 12 nm, which is 2 – 6 nm larger than that of original water domain. When the equilibrium is reached, the ACP spherules are separately stuck in the LCP structure, surrounded by squeezed surfactant chains, forming a fairly stable state.

While for high initial salt concentration (20 wt%, 30 wt%), the ACPs might meet and coalescence with each other before reaching the surfactant wall. The amorphous bulk they formed together occupies the water channel and cannot squeeze into surfactant wall since the contact area is quite large. Hence, they remain as the shapes of the water channel, forming long rods with a diameter ~ 6 nm. The ACP spherules with large diameter can also be formed. Yet the situation for them to meet before equilibrium and break the structure together has a higher possibility. Thus, the LCP structure is hard to keep in this case, and the crystallites start to emerge after 4 days.

5.2 Effect of GAGs during Aging

The effect of heparin can be explained in the following way: the possible adsorption of heparin molecules onto ACPs will disturb the rearrangement of Posner's clusters and therefore hinder the crystallization process. The electrostatic repulsion between the heparin chains may also keep the ACP spherules from coalescing, generating a better colloidal stability in the aging suspension. Thus, the crystallization of these nanometric spherules tends to occur locally, without interference from each other and form crystallites with a narrow size distribution. Furthermore, heparin molecules

might incorporate into the apatite structure during aging process, leading to local packing disorders.

5.3 Sample features: LCP vs. WBP

Each typical synthesis route endues the final products with distinct features. The samples obtained by LCP route had large aspect ratio and small crystallite size (~ 2 – 5 nm thick, 30 – 50 nm long), which not only raised the specific surface areas far more than 200 m^2/g but also abated samples' thermostability. Whereas the large crystallite size of WBP samples resulted in a better thermal performance.

Therefore, the disparity in the third stage (650 ℃–850 ℃) of the TGA/DSC curves of the LCP and WBP samples (Fig. 41) can be explained from two aspects. One is due to the relatively high proportion of ACP in WBP samples, which reveals the inferior controllability of WBP route. The other aspect is the difference in crystal size and crystallinity of LCP and WBP samples, yielding varying thermostability. It can be postulated that there would be exothermic peaks at an even higher temperature referring to the formation of TCP for WBP samples.

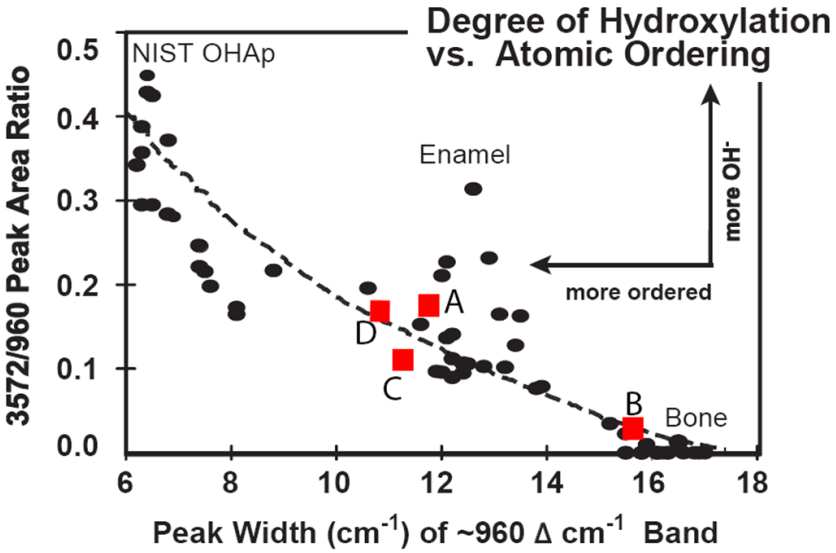

Figure 45: Comparison of Raman Spectra with Data of Various Synthetic and Biological HA Samples, by J. Bielecki.[56]

Fig. 45 shows the comparison between LCP and WBP samples and biological, geological, synthetic nano-crystalline and well-crystallized HA, based on the Raman spectra data performed by Pasteris, et al.[56] They noticed that for biological apatite, two particular expressions in Raman spectra are corresponding to the features of less atomic ordering and –OH deficiency: the peak width of the PO_4^{3-} vibration peak at ~960 cm^{-1} and the ratio between the areas of this peak and the O-H stretch peak. In this case, sample B (LCP, with GAGs) stands out from other synthetic HA and shows a great resemblance to bone apatite.

5.4 The Morphological Controllability: LCP vs. WBP

A schematic description of the LCP and WBP route particles during aging is presented

in Fig. 46. The contrast in controllability can be clearly seen. The LCP route provides nanometric ACPs with a narrow size distribution, as the starting "seeds". The following ACP – HA conversion for LCP samples is slow and can be regulated by several factors, such as temperature, pH and additives, etc. Furthermore, the aging can also be terminated at a specific stage by extracting the water media.

While for the WBP route, the particle formation process is less controlled. The large pH gradient at the early particle formation stage generates ACPs with a large size distribution and a great discrepancy in the ACP – HA conversion stage.

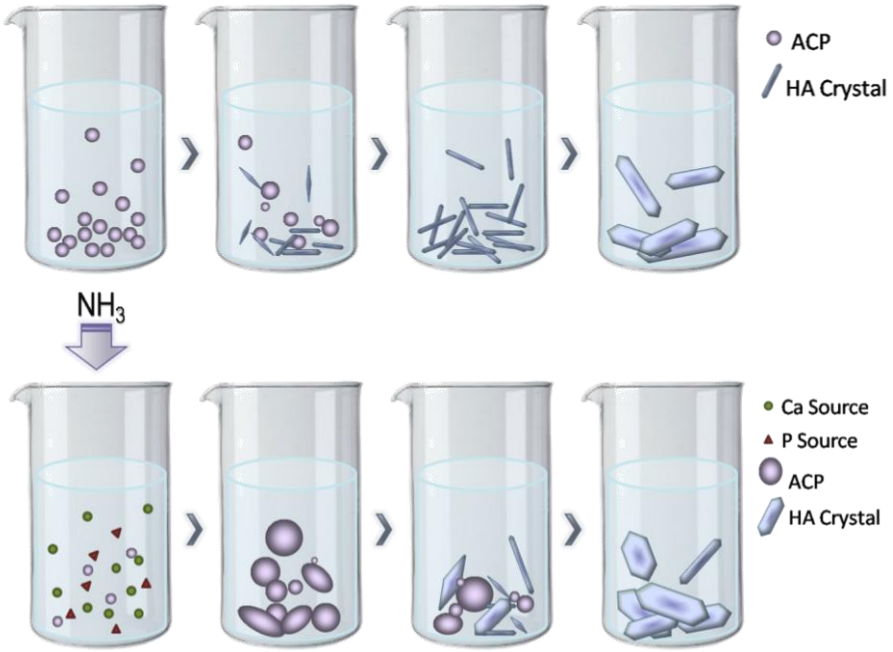

Figure 46: Illustration of LCP aging route (upper) vs. WBP route (bottom).

6 Conclusions

The H_2 LCP was proved to be an excellent template for the formation of unisize ACP spherules with a diameter of 8 – 12 nm.

The as-formed ACPs underwent "Induction, crystallization and crystal growth" in H_2O media. The ACP – HA conversion is temperature dependent and the aging time at room temperature is around 20 to 25 hours.

The addition of GAGs hindered the conversion to some extent.

LCP route showed better controllability than WBP. Combining the LCP route with controlled aging process, bone-like apatite with calcium and hydroxyl deficiency, carbonate substitution, extremely small crystal size and high specific surface area could be prepared.

6.1 Future Work

For the preparation of nanometric ACPs, other space-confining matrixes can be used as templates, such as L_α LCP, W/O micro-emulsion etc. It would be of interest to adjust the starting conditions to attain pure ACP nanowires. Moreover, Cubic LCP could be used as templates for the synthesis of mesoporous ACP.

For the ACP – HA conversion, improved morphological control can be achieved by prolonging the converting period, such as by aging at low temperature, involving other GAGs or additives.

It is also of great importance to investigate the applicability of prepared bone-like apatite as implant coatings. For such studies in vivo experiments should be conducted.

Finally, ACPs obtained from LCP route can be used as fillers in collagen or polymer matrixes. The in-situ crystallization of ACPs in the structural matrix might result bone-mimicing composites.

Acknowledgements

I would like to express my gratitude to the following people.

- Krister Holmberg and Johan Liu for providing me the opportunity to study at Chalmers.
- My supervisor Martin Andersson, for his guidance, support, inspiration through the whole year; and his heart poured into students, the cozy group environment and awesome Kickoff nights!
- Chris Knee and Johan Bielecki, for a great brainstorming and collaboration.
- Erik Nilsson, for the help with TEM, SAXS and PLM measurements.
- Romain Bordes, for the help with QCM-D measurements.
- All the people at Applied Surface Chemistry, for creating a pleasant and helpful atmosphere: Kurt Löfgren, Ann Jakobsson, Maria Claesson, Daniel Cederkrantz, Hannes Kannisto, Lisa Kylhammar, Adele Khavari, Alberta Mok…
- My dear friend Chang Shu and my family, for your care, company and trust.

References

1. E. Baer, et al. Hierarchical structure of collagen composite systems: Lessons from biology. In Biomimetics: Design and Processing of Materials, M. Sarikaya, ed., AIP Press, Woodbury NY, 1995, 13.
2. K. Anselme. Osteoblast adhesion on biomaterials. Biomaterials, 2000, 21:667-681.
3. M. Vallet-Regi, et al. Biomimetic Nanoceramics in clinical use From Materials to Applications. RSC Nanoscience & Nanotechnology, 2008.
4. R. Lakes. Materials with structural hierarchy. Nature, 1993, 361: 511-515.
5. S. Weiner, et al. Bone structure: From angstroms to microns. Journal of the Federation of American Societies for Experimental Biology, 1992, 6: 879-885.
6. J. D. Pasteris, et al. Bone apatite: The secret is in the carbonate. 2007 GSA Denver Annual Meeting, No. 109-5.
7. L. T. Kuhn, et al. Biomimetic strategies and materials processing. In Biomimetic Materials Chemistry, S. Mann, ed., Wiley-VCH, United Kingdom, 1996, 41-68.
8. S. Lees. A mixed packing model for bone collagen. Calcified Tissue International, 1981, 33: 591-602.
9. P. J. Thurner. Atomic force microscopy and indentation force measurement of bone. Nanomedicine and Nanobiotechnology, 2009, 1, 6: 624-649.
10. M. J. Olszta, et al. Bone structure and formation: A new perspective. Materials Science and Engineering R, 2007, 58: 77-116.
11. L. M. Rodriguez-Lorenzo, et al. Controlled crystallization of calcium phosphate apatites. Chemistry of Materials, 2000, 12: 2460-2465.
12. N. Rameshbabu, et al. Synthesis of nanocrystalline fluorinated hydroxyapatite by microwave processing and its in vitro dissolution study. Bulletin of Material Science, 2006, 29: 611-615.
13. W. Kim, et al. Mechanochemical synthesis of hydroxyapatite from $Ca(OH)_2$–P_2O_5 and CaO–$Ca(OH)_2$–P_2O_5 mixtures. Journal of Materials Science, 2000, 35: 5401-5405.
14. G. K. Lim, et al. Formation of nanocrystalline hydroxyapatite in nonionic surfactant emulsions. Langmuir, 1999, 15: 7472-7477.
15. C. Garcia, et al. Bioactive coatings prepared by sol–gel on stainless steel 316L. Journal of Non-Crystalline Solids, 2004, 348: 218-224.
16. M. I. Kay, et al. Crystal structure of hydroxyapatite. Nature, 1964, 204:1050-1051.
17. Web source: http://www.chemistry.upatras.gr/studs/sotk/hap.htm
18. R. A. Young. Some aspects of crystal structural modeling of biological apatites. Colloques internationaux C.N.R.S., Paris, 1975, 230, 21-39.
19. M. Banu. Mise en forme d'apatites nanocristallines: ceramiques et ciments. Thesis, Institut National Polytechnique de Toulouse, 2005.
20. X. Ranz. Développement et caractérisation de dépôts d'apatite obtenus par projection plasma sur prothèses orthopédiques. Thesis, Institut National Polytechnique de Toulouse, 1996.

21. E. Hayek, et al. Pentacalcium monohydroxyorthophosphate-hydroxylapatite. Inorganic Syntheses, 1963, 7: 63-65.
22. M. D. Grynpas, et al. Transient precursor strategy or very small biological apatite crystals? Bone, 2007, 41: 162-164.
23. H. A. Lowenstam, et al. Transformation of amorphous calcium phosphate to crystalline dahllite in the radular teeth of chitons. Science, 1985, 227: 51-53.
24. E. D. Eanes, et al. An electron microscopic study of the formation of amorphous calcium phosphate and its transformation to crystalline apatite. Calcified Tissue Research, 1973, 12: 143-158.
25. J. Melvin, et al. Recent studies of bone mineral: Is the amorphous calcium phosphate theory valid? Journal of Crystal Growth, 1981, 53 (1): 100-119.
26. N. C. Blumenthal, et al. Hydroxyapatite: Mechanism of formation and properties. Calcified Tissue Research, 1973, 13: 235-243.
27. J. Song, et al. Mineralization of synthetic polymer scaffolds: A bottom-up approach for the development of artificial bone. Journal of the American Chemical Society, 2005, 127: 3366-3372.
28. E. Bonucci, Ed. Calcification in Biological Systems. CRC Press, Boca Raton, Florida, 1992.
29. E. D. Eanes, et al. Intermediate states in the precipitation of hydroxyapatite. Nature, 1965, 208: 365-367.
30. A. L. Boskey, et al. Conversion of amorphous calcium phosphate to microcrystalline hydroxyapatite: A pH-dependent, solution-mediated, solid-solid conversion. The Journal of Physical Chemistry, 1973, 77 (19): 2313-2317.
31. A. S. Posner, et al. Synthetic amorphus calcium phosphate and its relationship to bone mineral. Accounts of Chemical Research, 1975, 8: 273-281.
32. X. Yin, et al. Biological calcium phosphates and Posner's cluster. Journal of Chemical Physics, 2003, 118 (8): 3717-3723.
33. J. C. Heughebaert, et al. Conversion of amorphous tricalcium phosphate into apatitic tricalcium phosphate. Calcified Tissue International, 1982, 34:S103-S108.
34. G. Montel, et al. New concepts in the composition, crystallization and growth of the mineral component of calcified tissues. Journal of Crystal Growth, 1981, 53: 74-99.
35. F. B. Rosevear. Liquid crystals: The mesomorphic phases of surfactant compositions. Journal of Cosmetic Chemistry, 1968, 19: 581-594.
36. W. Hamley. Liquid crystal phase formation by biopolymers. Soft Matter, 2010, 6: 1863.
37. C. Sanchez, et al. Biomimetism and bioinspiration as tools for the design of innovative materials and systems. Nature Materials, 2005, 4: 277-288.
38. S. A. Jewell, et al. Circularly polarised colour reflection from helicoidal structures in the beetle Plusiotis boucardi. New Journal of Physics, 2007, 9: 99.
39. Web source: http://www.bnl.gov/bnlweb/pubaf/pr/PR_display.asp?prID=07-X15
40. Web source: http://chemistry.caltech.edu/~fucose/Research%201.htm

41. Web source: http://themedicalbiochemistrypage.org/glycans.html
42. A. L. Boskey, et al. Effects of bone CS-proteoglycans, DS-decorin, and DS-biglycan on hydroxyapatite formation in a gelatin gel. Calcified Tissue International, 1997, 61: 298–305.
43. S. G. Rees, et al. Effect of serum albumin on glycosaminoglycan inhibition of hydroxyapatite formation. Biomaterials, 2004, 25: 971-977.
44. S. Chander, et al. Solubility and interfacial properties of hydroxyapatite: A review. D. N. Misra, ed., Plenum Press, 1984, 29-50.
45. P. Dechichi, et al. A model of the early mineralization process of mantle dentin. Micron, 2007, 38 (5): 486-491.
46. J. W. Goodby. Liquid crystal. phase transitions: Differential scanning calorimetry and optical microscopy. Web source: www.yorklc.com/docs/pdf/LCM.pdf
47. C. Bottier, et al. Galactosyl headgroup interactions control the molecular packing of wheat lipids in Langmuir films and in hydrated liquid-crystalline mesophases. Biochimica et Biophysica Acta. 2007, 1768: 1526-1540.
48. P. Alexandridis, et al. Self-Assembly of Amphiphilic Block Copolymers: The $(EO)_{13}(PO)_{30}(EO)_{13}$-Water-*p*-xylene System. Macromolecules, 1995, 28 (23): 7700-7710.
49. Web source: http://www.terrachem.de/en/roentgenbeugungsanalyse.php
50. Web source: http://www.microscopy.ethz.ch/interactions.htm
51. S. Brunauer, et al. Adsorption of gases in multimolecular layers. Journal of the American Chemical Society, 1938, 60: 309-319.
52. Q-Sense Basic Training, 2006. Web source: http://www.bu.edu/becf/downloads/BioInterface%20Technologies/QCMD/QCM-D%20Theory.pdf
53. S. G. Rees, et al. Interaction of glucuronic acid and iduronic acid-rich glycosaminoglycans and their modified forms with hydroxyapatite. Biomaterials, 2002, 23 (2): 481-489.
54. P. Kjellin, et al. (2005) Patent WO 2005/123579 A1.
55. J. C. Weber, et al. Electron microscope study of noncrystalline calcium phosphate. Archives of Biochemistry, 1967, 120: 723-724.
56. J. D. Pasteris, et al. Lack of OH– in nanocrystalline apatite as a function of degree of atomic order: implications for bone and biomaterials. Biomaterials, 2004, 25: 229-238.
57. Y. Miake, et al. Crystals in early porcine enamel. Calcified Tissue Research, 1993, 53: 249-256.
58. J. S. Earl, et al. Hydrothermal synthesis of hydroxyapatite. Journal of Physics: Conference Series, 2006, 26: 268-271.
59. P. Holmqvist, et al. Phase behavior and structure of ternary amphiphilic block copolymer-alkanol-water systems: comparison of poly(ethylene oxide)/ poly(propylene oxide) to poly(ethylene oxide)/poly(tetrahydrofuran) copolymers. Langmuir, 1997, 13: 2471-2479.